

# Atomic and Electronic Structure of the Al<sub>2</sub>O<sub>3</sub>/Al Interface during Oxide Propagation Probed by Ab Initio Grand Canonical Monte Carlo

Vrinda Somjit and Bilge Yildiz\*

Cite This: <https://doi.org/10.1021/acsami.2c08706>

Read Online

ACCESS |



Metrics &amp; More



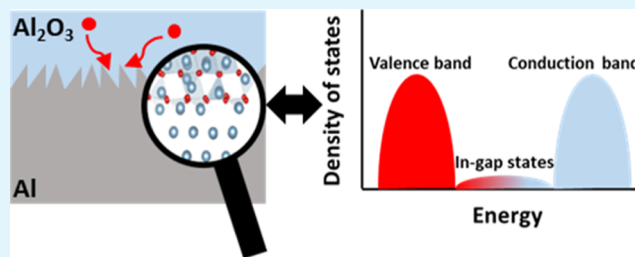
Article Recommendations



Supporting Information

**ABSTRACT:** Identifying the structure of the Al<sub>2</sub>O<sub>3</sub>/Al interface is important for advancing its performance in a wide range of applications, including microelectronics, corrosion barriers, and superconducting qubits. However, beyond the study of a few select terminations of the interface using computational methods, and top–down, laterally averaged spectroscopic and microscopic analyses, the explicit structure of the interface and the initial stages of propagation of the interface into the metal are largely unresolved. In this study, we utilize ab initio grand canonical Monte Carlo to perform a physically motivated, unbiased exploration of the interfacial composition and configuration space. We find that at equilibrium, the interface is atomically sharp with aluminum vacancies and propagates in a layer-by-layer fashion, with aluminum excess in the oxide layer at the interfacial plane. Oxygen incorporation, aluminum vacancy formation, and aluminum vacancy annihilation are the building blocks of Al<sub>2</sub>O<sub>3</sub> formation at the interface. The localized interfacial mid-gap states from under-coordinated aluminum atoms from the oxide and the immediate depletion of aluminum states near the Fermi level upon oxygen incorporation prevent oxygen dissolution ahead of the interface front and result in the layer-by-layer propagation of the interface. This is in sharp contrast to the ZrO<sub>2</sub>/Zr system, which forms interfacial sub-oxides, and also explains the favorable self-healing nature of the Al<sub>2</sub>O<sub>3</sub>/Al system. The occupied interfacial mid-gap states also increase the calculated n-type Schottky barrier heights. Additionally, we identify that interfacial aluminum core-level shifts linearly depend on the aluminum coordination number, whereas interfacial oxygen core-level shifts depend on long-range ordering at the interface. The detailed geometric and electronic insights into the interface structure and evolution expand our understanding of this fundamental interface and have important implications for the engineering and design of Al<sub>2</sub>O<sub>3</sub>/Al-based corrosion coatings with enhanced barrier properties, controllable transistor technologies, and noise-free superconducting qubits.

**KEYWORDS:** interface, ab initio, Monte Carlo, aluminum, oxide, corrosion, dielectric, barrier



## 1. INTRODUCTION

Aluminum oxide (Al<sub>2</sub>O<sub>3</sub>) and aluminum (Al) are two of the most foundational industrial materials and have the largest weight-share of the ceramics<sup>1</sup> and base metal<sup>2</sup> world market, respectively. This is due to their excellent properties: the extreme hardness, electrical resistivity, corrosion resistance, refractoriness, and biocompatibility of Al<sub>2</sub>O<sub>3</sub>; and, at the other end of the spectrum are the high formability, thermal conductivity, and low density of Al. Used together, the aluminum oxide/aluminum (Al<sub>2</sub>O<sub>3</sub>/Al) interface is of significant fundamental and practical importance in a wide range of technological applications, such as corrosion barriers,<sup>3</sup> superconducting qubits,<sup>4</sup> micro-/nano-electronics,<sup>5</sup> and catalysis.<sup>6</sup> The interfacial structure can play a critical role in determining the performance of the above applications. For example, reactions at the Al<sub>2</sub>O<sub>3</sub>/Al interface, such as aluminum/oxygen vacancy formation and annihilation and exchange of electrons and holes, are important for Al<sub>2</sub>O<sub>3</sub> passive film growth.<sup>7</sup> Defects at the interface, such as carbon

and hydrogen,<sup>9</sup> can alter interfacial adhesion, which can impact its susceptibility to spallation. In the context of electronics, two-level systems at the interface, such as oxygen vacancies<sup>10</sup> and hydrogen interstitials,<sup>11</sup> are hypothesized to be sources of noise and decoherence in superconducting qubits. Trapping/detrapping of electrons at the aluminum oxide/Al electrode interface<sup>12</sup> in resistive switching devices, Fermi level pinning at the aluminum oxide/Al interface in metal-oxide-semiconductor (MOS) devices,<sup>5</sup> and Schottky barrier height (SBH) changes in Al/Al<sub>2</sub>O<sub>3</sub>/Al tunnel junctions<sup>13</sup> can alter the device behavior

Received: May 16, 2022

Accepted: August 30, 2022

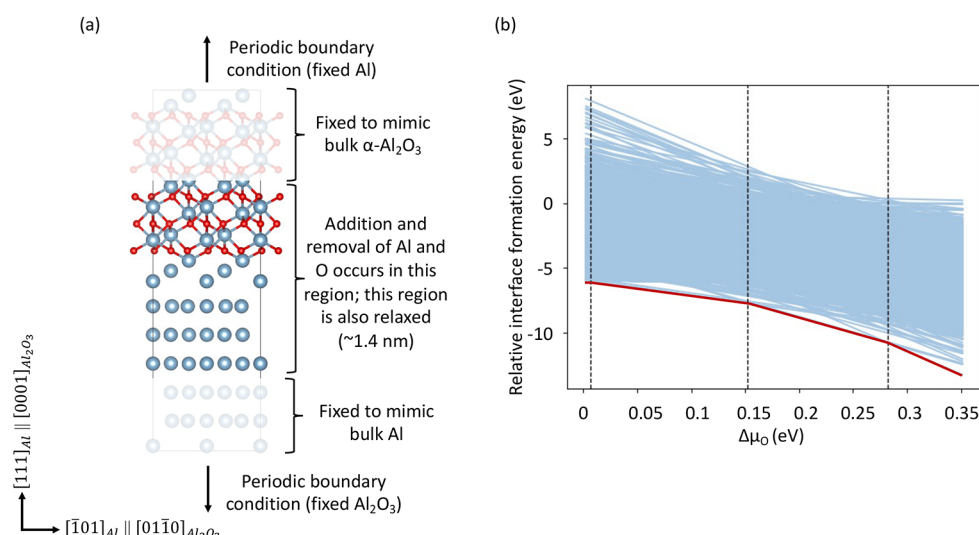


**Figure 1.** (a)  $\alpha$ - $\text{Al}_2\text{O}_3(0001)/\text{Al}(111)$  interface model used in GCMC simulations. This is the idealized starting structure which is used as a reference, while calculating relative interface formation energies. Blue and red spheres correspond to Al and O atoms, respectively. The relaxed interfacial and fixed bulk regions are marked. Further details can be found in the [Computational Methods Section](#). (b) Relative interface formation energy as a function of  $\Delta\mu_{\text{O}}$  for all the interface structures accepted by GCMC. The lowest interface formation energies are denoted with a thick, maroon line. The transition  $\Delta\mu_{\text{O}}$  is marked with dotted lines.

such as bipolar switching, threshold voltages, and tunneling currents, respectively.

Given this importance of the  $\text{Al}_2\text{O}_3/\text{Al}$  interface, significant experimental and computational effort has gone into understanding the structure and growth of  $\text{Al}_2\text{O}_3$  on Al. Environmental transmission electron microscopy<sup>14</sup> of the oxide morphology during oxidation of the Al surface has established that oxide growth occurs primarily via island nucleation at lattice kinks, followed by lateral island growth and oxide propagation into the metal.<sup>14</sup> Controlled thermal oxidation of aluminum surfaces<sup>15,16</sup> have concluded that crystalline oxide grows epitaxially on Al.<sup>15</sup> X-ray photoelectron spectroscopy (XPS) studies<sup>17,18</sup> report an interfacial Al 2p oxidic peak, which has been attributed to deficiently coordinated Al cations at the interface. However, these experiments primarily focus on the morphological changes in the oxide during the initial surface oxidation regime, rely on top-down, laterally-averaged spectroscopy and microscopy techniques, and do not explicitly characterize the structure of the buried interface. The atomic and electronic structure of the oxide layer(s) at the interface remain unresolved. In particular, identifying the interfacial equilibrium concentrations and preferred positions of Al and O atoms (such as the possibility of Al/O interfacial excess and whether O dissolves into Al ahead of the interface plane as is observed in the  $\text{ZrO}_2/\text{Zr}$  system<sup>19,20</sup>) is still an open question. Moreover, the structural and electronic changes that take place at the interface as the oxide advances into the metal (especially beyond the initial surface oxidation regime) remain largely unclear.

Computational studies have investigated the  $\text{Al}_2\text{O}_3/\text{Al}$  interface using density functional theory (DFT) and molecular dynamics (MD). First principles studies have primarily focused on identifying stable oxide terminations at the interface,<sup>21,22</sup> thickness-dependent phase stability of  $\text{Al}_2\text{O}_3$  on Al,<sup>23</sup> and evaluating properties such as the work of adhesion<sup>8,24</sup> and tunneling efficiency across Al/ $\text{Al}_2\text{O}_3$ /Al tunnel junctions.<sup>25</sup> DFT studies have also investigated the early stage growth of the oxide on Al,<sup>26–28</sup> proposing a barrierless mechanism for

the initial oxidation of Al via Al extraction by adsorbed oxygen atoms<sup>26</sup> and identifying the favorable surface and subsurface sites for oxygen adsorption.<sup>27,28</sup>  $\text{Al}_2\text{O}_3$  growth on Al has been studied using ab initio<sup>29</sup> and classical MD<sup>30,31</sup> as well, by sequentially adding  $\text{O}_2$  molecules over the Al surface. However, the open questions from experiments mentioned above remain unanswered by prior computational work as well. Namely, understanding of the equilibrium atomic structure of the interface, interfacial Al and O concentrations and preferential positions, atomistic processes and electronic structure changes at the interface as the oxide advances into the metal beyond the initial surface oxidation regime, and the effect of the interface configuration on electronic properties, is still lacking. Moreover, the prior computational studies rely on significant approximations. In particular, ab initio studies usually limit the investigation to only two layers of O adsorption on Al,<sup>26–29</sup> hand-select oxygen incorporation sites,<sup>26,27</sup> and study only select terminations of  $\text{Al}_2\text{O}_3$  on Al.<sup>21,23,28</sup> MD studies usually rely on artificially high  $p_{\text{O}_2}$  to enhance dynamics<sup>31</sup> and may be limited by kinetic barriers.<sup>25,29–31</sup> Neither DFT nor MD studies systematically study different stoichiometries at the interface due to the large number of compositional possibilities. The interfacial composition and configuration phase space are vast, and therefore, the above approximations that rely on manual construct may overlook the true, equilibrated structure of the interface.

In this paper, we identify the equilibrium  $\text{Al}_2\text{O}_3/\text{Al}$  interface structure and initial stages of  $\text{Al}_2\text{O}_3$  propagation into Al metal using ab initio grand canonical Monte Carlo (GCMC). A key advantage of ab initio GCMC is that by stochastically inserting/removing atoms and relaxing the structure, the simulation is able to explore a drastically wide configuration and chemical space. This enhances ergodicity. Moreover, the simulation samples the configurations according to the Boltzmann distribution at a given realistic chemical potential and temperature to find the structures favored at thermodynamic equilibrium. Thus, this enables a physically motivated, unbiased exploration of the configuration space. This method

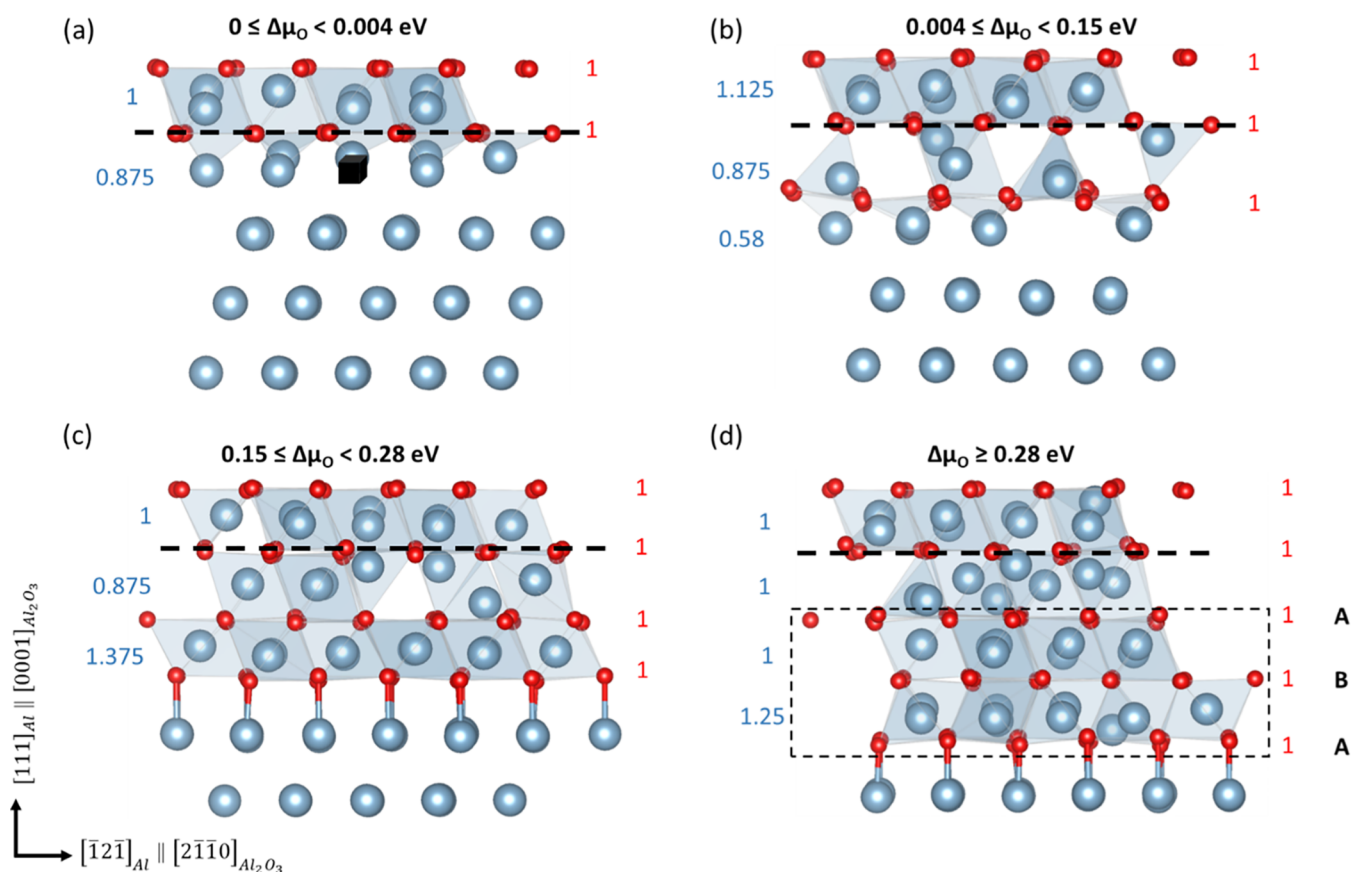


**Figure 2.** (a–d) Interface structures with the lowest interface formation energies across  $\Delta\mu_{\text{O}}$ . Only layers near the interface are shown. The location of the original interface oxygen plane is marked with a black dashed line. Blue spheres represent aluminum atoms, and red spheres represent oxygen atoms. The black cube denotes an aluminum vacancy. Layer-wise aluminum coverage is marked in blue on the left, and oxygen coverage is marked in red on the right of each structure. In (d),  $\text{Al}_2\text{O}_3$  formed at the interface is marked with a dotted box, and the A–B–A HCP stacking formed by oxygen layers is also denoted on the right.

has recently been used to study oxidation of the Ag (111) surface<sup>32</sup> and to compute the average hydrogen excess at vacancies in FCC metals.<sup>33</sup> We extend this promising new method to a solid/solid interface in this study. At the outset, it seems contradictory to employ equilibrium arguments to a kinetically determined process like Al oxidation. While the oxidation of Al is indeed kinetically limited over long length-scales due to the low electronic and ionic conductivity of  $\text{Al}_2\text{O}_3$ , interfaces (like  $\text{Al}_2\text{O}_3/\text{Al}$ ) in general present short length-scales and are efficient sources and sinks for point defects. These factors can cause the kinetics at the interface to be rapid enough such that the local equilibrium can be reached, allowing the application of equilibrium thermodynamics concepts, as in this study. Moreover, such thermodynamic analysis is critical, as equilibrium states and their relative stabilities frequently dictate the rate (or kinetics) of a process.

By performing ab initio GCMC at different oxygen chemical potentials ( $\mu_{\text{O}}$ ), we identify the equilibrium interface structure and the thermodynamically stable structures as  $\text{Al}_2\text{O}_3$  grows into the aluminum metal. Examining the GCMC trajectory enables us to identify the local events that lead to oxide formation at the interface. We also analyze the electronic structure of the obtained interfaces, in terms of the density of states, SBHs, and core-level shifts. By connecting our electronic and geometric analyses, our findings provide new insights into the initial stages of  $\text{Al}_2\text{O}_3$  propagation into Al, help understand multiple experimental hypotheses and trends, and have

implications for the performance and engineering of the fundamental  $\text{Al}_2\text{O}_3/\text{Al}$  interface in its different technological applications.

## 2. RESULTS

**2.1. Equilibrium Atomic Structures and Stoichiometries at the Interface as a Function of  $\Delta\mu_{\text{O}}$ .** Figure 1a shows the interface model used in our GCMC simulations, which is described in detail in the [Computational Methods Section](#). Figure 1b shows the relative interface formation energy as a function of  $\Delta\mu_{\text{O}}$  for all the configurations ( $\sim 2000$ ) accepted by the different GCMC runs carried out at various  $\mu_{\text{O}}$  at 800 K. Each blue line corresponds to the DFT calculation of a trial configuration accepted by GCMC (i.e., calculation of  $E_{\text{system}}$  in eq 6). We see that the envelope (thick maroon line in Figure 1b) denoting the lowest relative interface formation energies comprises four regions. The structures corresponding to the four regions are shown in Figure 2a–d. Layer-wise oxygen and aluminum “coverage” [i.e., the ratio of the number of oxygen and aluminum atoms present per layer near the interface to that present per layer in bulk  $\alpha\text{-Al}_2\text{O}_3$  (12 and 8, respectively)] are also indicated on the right and left, respectively. All structures are generated with VESTA.<sup>34</sup>

From  $0 \leq \Delta\mu_{\text{O}} < 0.004$  eV, the interface favors 12.5% aluminum vacancies on the oxide side (the vacancy is denoted as a black cube in Figure 2a). From  $0.004 \leq \Delta\mu_{\text{O}} < 0.15$  eV, the interface favors one monolayer of oxygen incorporated at

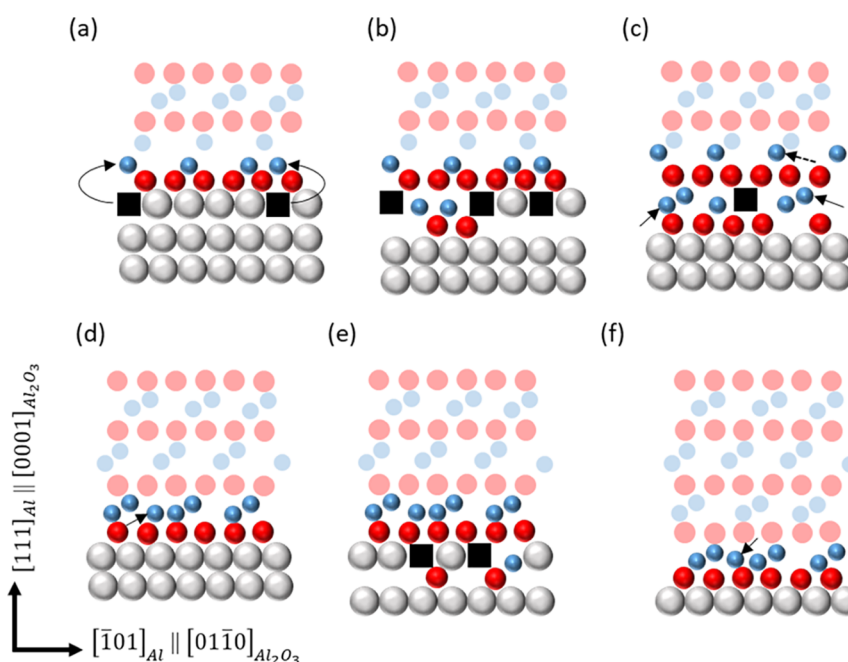


**Figure 3.** Evolution pathway followed by GCMC to form  $\text{Al}_2\text{O}_3$  upon oxidation of aluminum metal layers near the interface. Red spheres represent oxygen, blue spheres represent oxidized aluminum atoms, grey spheres represent aluminum metal atoms, and black squares indicate aluminum vacancies. (a) Oxygen incorporation leads to aluminum extraction (indicated by arrows) from the metal layer at the interface, leading to aluminum vacancies in the metal layer. (b) Oxygen incorporation also leads to oxidation of Al metal atoms and formation of additional aluminum vacancies in the metal layer at the interface. (c) Further oxygen incorporation leads to annihilation of aluminum vacancies by addition of aluminum back to the interstitial sites (marked by solid arrows) at the oxidizing interface plane. This also leads to change in Al coordination from tetrahedral to octahedral in the Al layer above the oxidizing interface plane (marked with a dashed arrow). (d) Complete oxygen incorporation in this layer leads to aluminum excess at the oxide side of the interface plane (marked with a solid arrow). (e) Oxygen incorporation leads to aluminum vacancy formation in the interfacial metal plane and oxidation of metal atoms. (f) Complete oxygen incorporation in this layer leads to aluminum excess in the oxide side of the interface plane (marked with a solid arrow) and stoichiometric number of aluminum in the plane above the oxidized interfacial plane. This is a simplified schematic; the actual structures generated during the evolution trajectory can be found in [Supporting Information Note S2](#).

the FCC sites of the metal layer at the interface. As seen in [Figure 2b](#), aluminum is extracted from the interfacial metal layer and forms Al–O tetrahedra. Given that the structures in [Figure 2a,b](#) are close in energy at  $\Delta\mu_{\text{O}} = 0$  eV, it is possible that both these structures occur at equilibrium. From  $0.15 \leq \Delta\mu_{\text{O}} < 0.28$  eV, another complete layer of oxygen is incorporated at the interface at the tetrahedral B (tB) interstitial sites of the metal layer, and the interface aluminum plane at the oxide side has an aluminum excess of  $\sim 37.5\%$  compared to stoichiometric  $\text{Al}_2\text{O}_3$  (seen in [Figure 2c](#)). Note that aluminum atoms in the oxide side of the interface are now primarily octahedrally coordinated, compared to the predominant tetrahedral Al–O coordination in [Figure 2b](#). At  $\Delta\mu_{\text{O}} \geq 0.28$ , another complete oxygen layer is incorporated at the interface at the tB interstitial sites of the metal layer. The interface aluminum plane at the oxide side is once again Al-rich, with an aluminum excess of  $\sim 25\%$  compared to stoichiometric  $\text{Al}_2\text{O}_3$  (seen in [Figure 2d](#)), and the interfacial aluminum atoms in the oxide side are octahedrally coordinated. Importantly, the aluminum plane above the interface oxide plane (which previously had an aluminum excess of 37.5%, as shown in [Figure 2c](#)) has regained its stoichiometry. Moreover,  $\text{Al}_2\text{O}_3$  is now formed at the interface (highlighted with the dotted box), with oxygen forming a hexagonal close-packed lattice (note the A–B–A stacking) and aluminum primarily occupying the octahedral interstitial sites.

The findings above reveal a number of important properties of the  $\text{Al}_2\text{O}_3/\text{Al}$  interface and the thermodynamically stable

structures that form during its propagation. In all cases, the interface is atomically sharp. Interface propagation occurs in a layer-by-layer fashion, with no oxygen penetration into the aluminum metal layer ahead of the oxide/metal interface. Oxygen is incorporated in the next metal layer only after saturating the preceding layer. Structures with partial coverages of oxygen per layer are not stable, that is, at a given  $\Delta\mu_{\text{O}}$ , the structure with a complete monolayer of oxygen per layer has lower interface formation energy (and is therefore more stable and will preferentially occur) than any other structure with  $<1$  monolayer of oxygen per layer. The aluminum plane at the oxide side of the propagating interface is always Al-rich and regains its stoichiometry once oxygen is incorporated in the next layer. Moreover, the Al–O coordination changes from tetrahedral to octahedral as oxygen is incorporated in successive aluminum metal layers, and  $\text{Al}_2\text{O}_3$  is fully formed only after three layers of oxygen incorporation into the aluminum metal. Thus, the interface does not propagate as  $\text{Al}_2\text{O}_3$ ; instead, it forms  $\text{Al}_2\text{O}_3$  when at least three metal layers near the interface oxidize.

**2.2. Building Blocks for  $\text{Al}_2\text{O}_3$  Formation at the Interface.** The relative interface formation energy plot in [Figure 1b](#) reveals the thermodynamically stable interface structures as  $\Delta\mu_{\text{O}}$  is gradually increased. However, it does not show the mechanism behind the formation of these structures. Examination of the GCMC trajectory provides insights into the evolution of the stable structures, that is, the building blocks and local events caused by oxygen incorpo-

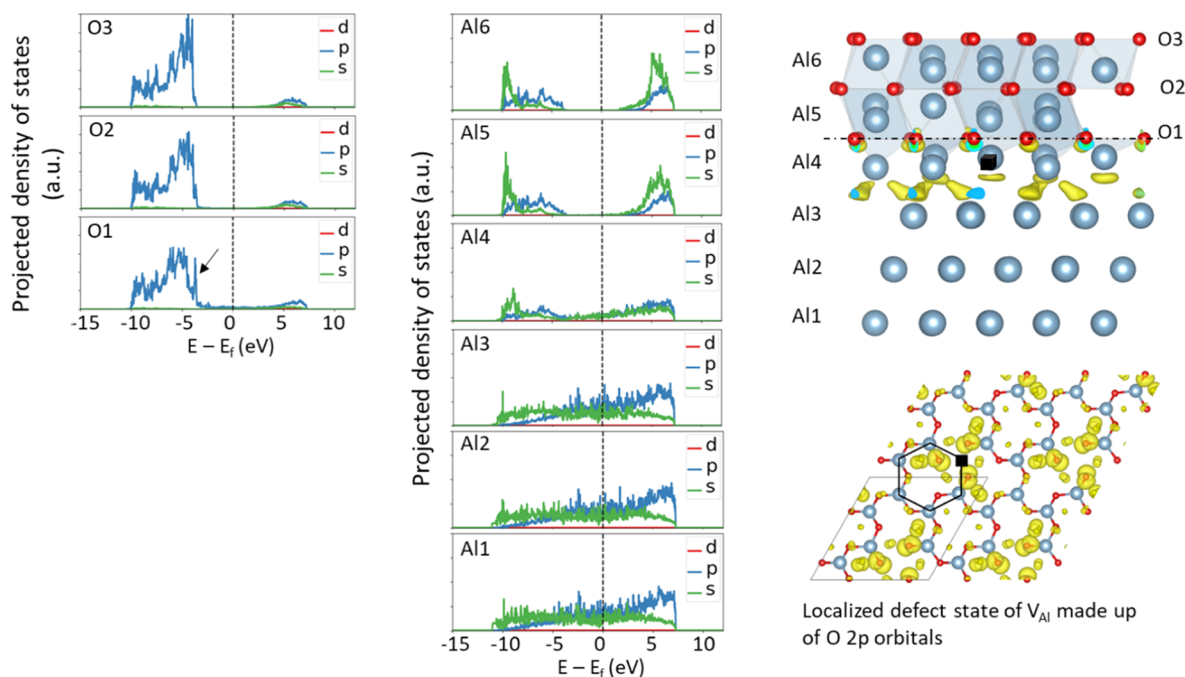


**Figure 4.** Layer-wise PDOS and partial charge density profiles of the occupied mid-gap states of configuration 1. The location of the original interface oxygen plane is marked with a black dotted-dashed line on the partial charge density profile. The partial charge density of the defect state corresponding to the aluminum vacancy at the interface is also shown. Note that the partial charge density profiles of the occupied mid-gap states have a minor, finite contribution from MIGS; however, these are not seen in the plots because their density is low compared to the contribution of under-coordinated Al to the mid-gap states. The dotted line on the PDOS plot marks the Fermi level. Isosurface = 0.01 electrons/Å<sup>3</sup>. PDOS scale is the same in Figures 4–7.

ration, which lead to interfacial advancement. Figure 3 shows a schematic of the key stages of the evolution pathway, elucidating the processes that take place at the interface during oxide growth into the Al metal.

In general, oxygen incorporation leads to aluminum deficiency in the metal layer at the interface, either via aluminum extraction or by the formation of aluminum vacancies (Figure 3a,b). Further oxygen incorporation in the aluminum metal layer then leads to addition of aluminum back to the interstitial sites of the Al-deficient metal plane (Figure 3c), thus annihilating the aluminum vacancies and ultimately causing aluminum excess at the (now oxidized) interface aluminum plane (Figure 3d) and change in Al–O coordination from tetrahedral to octahedral in the aluminum plane above the interfacial oxide plane (Figure 3c). Oxygen incorporation in the next layer follows the same cycle of oxygen incorporation → aluminum vacancy formation in the interfacial metal layer (Figure 3e) → further oxygen incorporation → aluminum interstitial addition and vacancy annihilation at the oxidizing interface metal plane → aluminum excess at the oxidized interfacial plane and ultimately resulting in the stoichiometric number of aluminum in the layer above the oxidized interfacial plane (Figure 3f).

Encouragingly, this examination of the GCMC evolution pathway matches hypotheses from experiments<sup>35</sup> and crystallographic theory analysis,<sup>7,36</sup> which propose that aluminum vacancies and oxygen are incorporated at the interface metal plane during oxide growth via counter-diffusion of oxygen and aluminum through Al<sub>2</sub>O<sub>3</sub>, and interfacial aluminum vacancies are annihilated by injecting vacancies into the metal sink.<sup>7,36</sup> This study reveals the atomic structures obtained during such scale/metal reactions at the interface. The relaxed structures and local rearrangements that resemble Al<sub>2</sub>O<sub>3</sub> generated during

this evolution trajectory can be found in Supporting Information Note S2.

Note that the thermodynamically stable phases that make up the lowest energy envelope, as shown in Figure 1b, always have complete monolayers of oxygen in each layer, that is, interfacial configurations with partial coverages of oxygen in each layer always have higher interface formation energies and therefore are never stable. This seems counter-intuitive as one would expect the oxygen coverage per layer to increase gradually with increasing  $\mu_{\text{O}}$  due to the energy cost of incorporating additional oxygen atoms. As explained in detail by Finnis et al.,<sup>37</sup> this trend is because point defects (such as aluminum vacancies and interstitials as seen in Figure 3), combined with structural relaxation and rearrangements upon oxygen incorporation, cause the structures with complete monolayers of oxygen in each layer to resemble Al<sub>2</sub>O<sub>3</sub> most closely. These structures therefore overcome the energy cost of incorporating additional oxygen atoms<sup>37</sup> and have the least energy and are the most stable compared to interfacial configurations with partial oxygen coverages per layer.

Note that although Al<sub>2</sub>O<sub>3</sub> forms at the interface upon incorporation of the third oxygen layer, the positions of some of the aluminum atoms in the oxide side of the interface are different from that of Al in bulk  $\alpha$ -Al<sub>2</sub>O<sub>3</sub> ( $\alpha$ -Al<sub>2</sub>O<sub>3</sub> is the only thermodynamically stable polymorph of Al<sub>2</sub>O<sub>3</sub>). For example, the Wyckoff positions of several octahedral interstitial Al atoms are different from that of Al in bulk  $\alpha$ -Al<sub>2</sub>O<sub>3</sub>. We discuss the possible reasons behind this (such as the effect of strain and presence of mid-gap states within the Al<sub>2</sub>O<sub>3</sub> band gap near the interface) in Supporting Information Notes S4 and S5; however, we emphasize here that the main results of this section (layer-wise propagation of the interface, aluminum excess at the oxide side of the interface plane, and oxygen

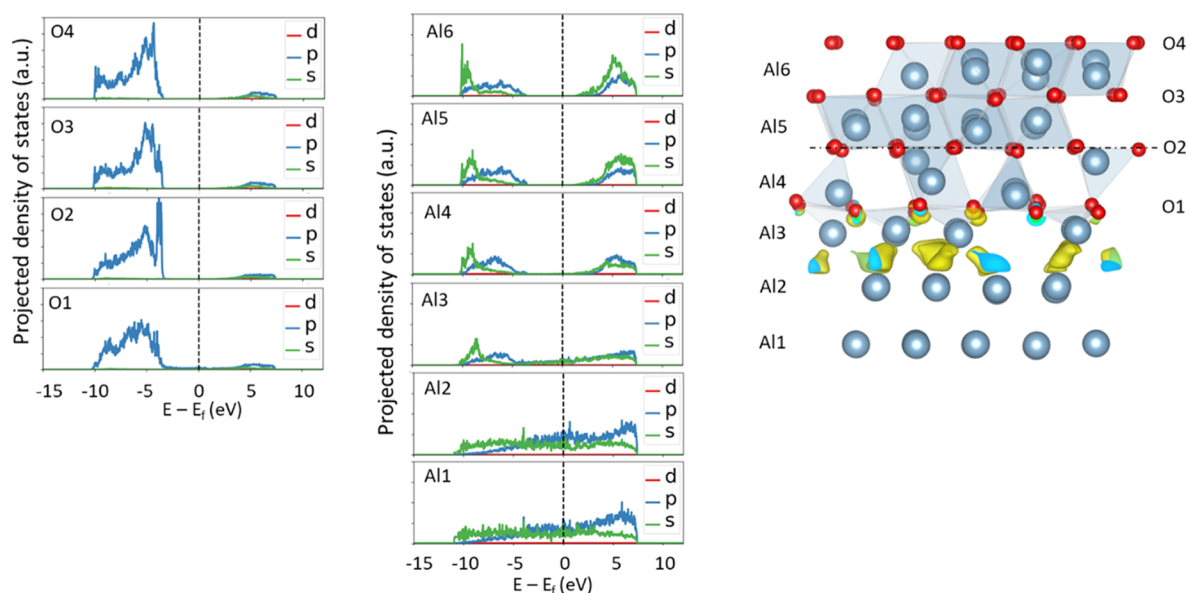


**Figure 5.** Layer-wise PDOS and partial charge density profiles of the occupied mid-gap states of configuration 2. Isosurface =  $0.009 \text{ eV}/\text{\AA}^3$ .

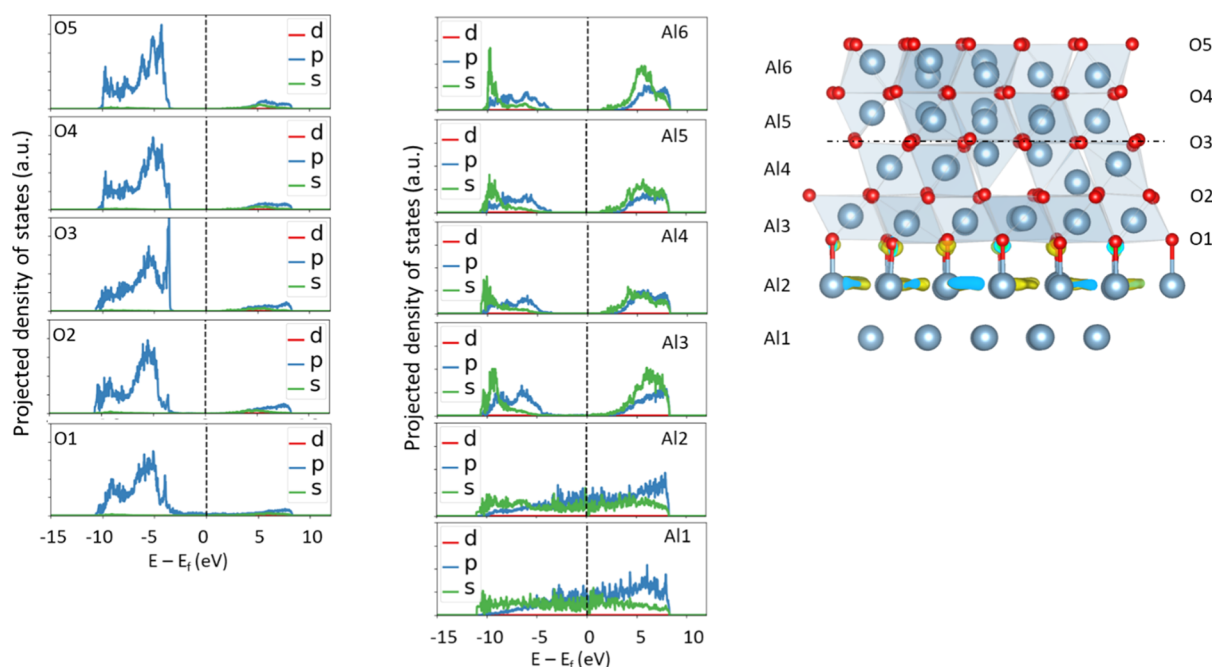


**Figure 6.** Layer-wise PDOS and partial charge density profiles of the occupied mid-gap states of configuration 3. Isosurface =  $0.01 \text{ electrons}/\text{\AA}^3$ .

incorporation  $\rightarrow$  aluminum vacancy formation  $\rightarrow$  aluminum interstitial addition  $\rightarrow$  aluminum vacancy annihilation being the local building blocks for interfacial evolution) still hold.

**2.3. Electronic Structure Analysis of Equilibrium Interfacial Structures.** Figures 4–7 show the layer-wise partial densities of states (PDOS) of the thermodynamically stable configurations discussed in Section 2.1 and the corresponding partial charge density plots of their occupied mid-gap states. Each layer of aluminum and oxygen and their corresponding PDOS panel are labeled Al1–Al6 and O1–O6, respectively. In all cases, we find a finite, continuous distribution of states in the band gap of  $\text{Al}_2\text{O}_3$  at the interface. These gap states are interfacial states, primarily made of O 2p and hybridized Al 3sp orbitals of the atoms from  $\text{Al}_2\text{O}_3$  at the interface, decaying away from the interface. The  $\text{Al}_2\text{O}_3$  bulk

band gap is regained from the second or third Al/O layer away from the interface. The interfacial states also have a minor contribution from the extended states of Al metal (metal induced gap states, i.e., MIGS) as the latter has continuous DOS present within the  $\text{Al}_2\text{O}_3$  band gap. The gap states below the Fermi level are occupied, despite these energies being formally forbidden in bulk  $\text{Al}_2\text{O}_3$ . Additionally, for all the configurations, the PDOS profiles of the oxygen layer near the interface (labeled O1) do not match those of oxygen in bulk  $\alpha$ - $\text{Al}_2\text{O}_3$ . Instead, the features look like those of oxygen in  $\gamma$ - $\text{Al}_2\text{O}_3$ ,<sup>38</sup> likely due to the presence of threefold coordinated oxygen at the interface.

Here, we highlight the specific aspects of the PDOS profiles for each configuration:

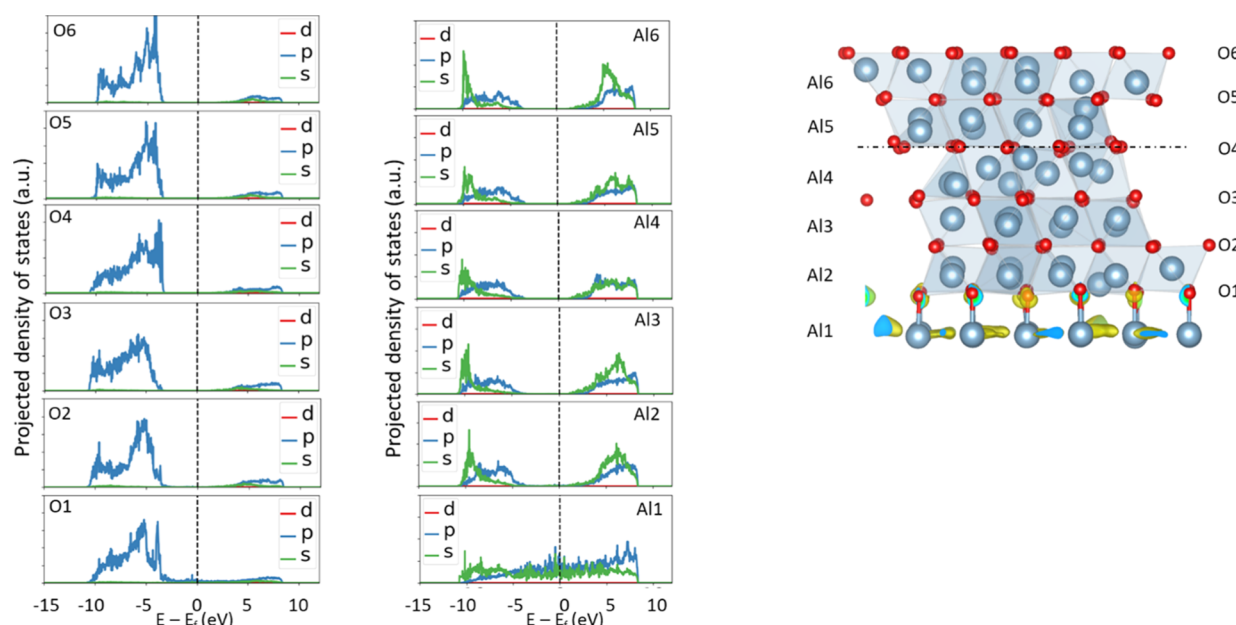


**Figure 7.** Layer-wise PDOS and partial charge density profiles of the occupied mid-gap states of configuration 4. Isosurface = 0.009 electrons/Å<sup>3</sup>.

(i) Configuration 1 (Figure 4) and configuration 2 (Figure 5) have similar PDOS and partial charge density profiles. Bader charge analysis (see Supporting Information Note S3) reveals that the interfacial Al atoms on the oxide side (layer Al4 and Al3 in Figures 4 and 5 respectively) on average each have one extra electron (compared to Al<sup>3+</sup>) due to under-coordination. These extra electrons are accommodated in the mid-gap states made of Al 3s, 3p, and O 2p from the oxide layer near the interface, as seen in panels O1 and Al4 (Figure 4) and panels O1 and Al3 (Figure 5) of the layer-wise PDOS and the partial charge density plot of the occupied mid-gap states. Interestingly, the partial charge density plots in Figures 4 and 5 also reveal that the orientation of the hybridized Al 3sp charge densities are at 90° to each other, mimicking the octahedral Al–O coordination in Al<sub>2</sub>O<sub>3</sub>. By comparing the location of the Al 3sp charge density in Figure 4 and the location of oxygen in layer O1 in Figure 5, it is clear that this localized charge density dictates the positions where oxygen incorporates in the next layer. Additionally, the interface in configuration 1 has 12.5% Al vacancies on the oxide side. These are localized defect states, made of O 2p orbitals of layer O1, as shown in the O PDOS peak at  $\sim -3.7$  eV and in the defect partial charge density plot in Figure 4. Finally, in configuration 2, the PDOS profiles of the aluminum layer extracted due to oxygen incorporation (layer Al4) and layer Al3 matches closely with that of aluminum in Al<sub>2</sub>O<sub>3</sub>, with localized Al 3sp states beginning to be seen in the energy ranges from  $-5$  to  $-10$  eV and  $+3$  to  $+7$  eV. Thus, addition of just one layer of oxygen can rapidly change the electronic structure of aluminum metal near the interface (i.e., localizing Al 3sp states and decreasing the density of states near the Fermi level), and can start to form Al<sub>2</sub>O<sub>3</sub> at the interface.

(ii) Configurations 3 (Figure 6) and 4 (Figure 7) have PDOS and partial charge density profiles similar to each other but slightly distinct from configurations 1 and 2. In both cases, we see that the contribution to the mid-gap states primarily comes from O 2p orbitals at the interface. The contribution of Al 3sp orbitals to the density of mid-gap states is lower than that of configurations 1 and 2, which is likely due to the

complete coordination of Al at the interface (layer Al3 and Al2 in Figures 6 and 7, respectively). Importantly, this shows that for the Al<sub>2</sub>O<sub>3</sub>/Al interface, under-coordinated interfacial Al atoms from the oxide largely determine the density of mid-gap states at the Al<sub>2</sub>O<sub>3</sub>/Al interface vs that of other phenomena like MIGS. However, MIGS still contribute to a minor, finite density of states in these interfacial Al layers. In fact, excess Al interstitials introduce additional electrons that are accommodated in defect levels near the conduction band minimum in bulk Al<sub>2</sub>O<sub>3</sub> (see Supporting Information Note S4). Thus, it is possible that unoccupied mid-gap states contributed by MIGS stabilize the excess aluminum interstitials found at the interfacial Al plane in the oxide side by accommodating additional electrons introduced by the excess Al interstitials.

Note that we do not observe such excess Al in configurations 1 and 2 as the oxidized Al plane (layer Al5 and Al4 in Figures 4 and 5, respectively) is considerably farther away from the Al metal layer ( $\sim 4$  Å) than layer Al3 (Al2) in Figure 6 (Figure 7) ( $\sim 3$  Å) and thus likely do not feel the stabilizing effect of MIGS. Furthermore, although Al occupies the octahedral interstitial sites of the HCP lattice created by O, as shown in Figure 7 (similar to bulk  $\alpha$ -Al<sub>2</sub>O<sub>3</sub>), the Wyckoff positions of several Al atoms are different from that of Al in bulk  $\alpha$ -Al<sub>2</sub>O<sub>3</sub>. It is possible that the presence of mid-gap states within the Al<sub>2</sub>O<sub>3</sub> band gap near the interface stabilize these sites. Additionally, the charge density is seen in the tetrahedral sites of the Al metal layer at the interface, made of hybridized Al 3sp orbitals. By comparing the location of the Al 3sp charge density in Figure 5 (Figure 6) and the location of oxygen in layer O1 in Figure 6 (Figure 7), it is clear that this localized charge density dictates the positions where oxygen incorporates in the next layer.

It is important to emphasize here that the DOS analyses above employed the Perdew–Burke–Ernzerhof (PBE) parameterization of the generalized gradient approximation (GGA)<sup>39</sup> exchange–correlation functional, which is known to have limited accuracy in describing the electronic structure of materials. We already see charge localization at the interface (such as due to under-coordinated Al) with this approximate

functional; however, for applications such as investigating noise in Al/Al<sub>2</sub>O<sub>3</sub>/Al superconducting qubits,<sup>40</sup> accurately modeling the electron correlation and localization of MIGS at the interface with higher-order functionals will be critical.

In total, in all cases, we see that incorporation of oxygen rapidly changes the electronic structure of aluminum metal at the interface. The mid-gap states are interfacial states, primarily made up of the O 2p and Al 3sp orbitals of the oxide. Thus, these are Bardeen states,<sup>41</sup> that is, semiconductor surface states, which may influence the Fermi level alignment and thus the effective work function of Al, SBH of the interface, cause deviation from the Mott–Schottky rule, and may also explain the scatter in experimentally measured SBHs. The contribution of MIGS to this interface is minor; however, MIGS likely plays a role in stabilizing the interfacial Al excess and Al occupation in different Wyckoff positions. Moreover, from the orientation and localization of the Bardeen states seen in the partial charge density plots of Figures 4–7, it is clear that these states likely cause the layer-by-layer advancement of the interface to form Al<sub>2</sub>O<sub>3</sub> by dictating where subsequent oxygen incorporates at the interface.

**2.4. Effect of the Interfacial Composition on the Schottky Barrier Height.** It is now well established that the SBH can strongly depend on the atomic structure and chemistry of the metal/semiconductor interface.<sup>42</sup> We investigated this dependence of the SBH on the interface composition to understand the factors that may govern the SBH at the Al<sub>2</sub>O<sub>3</sub>/Al interface and give insights into possible ways to engineer it. This is relevant for its use in applications such as superconducting qubits, resistive switching devices, and radiation detectors.

Figure 8 shows the calculated n-type SBH (n-SBH) as a function of the total number of oxygen atoms incorporated in

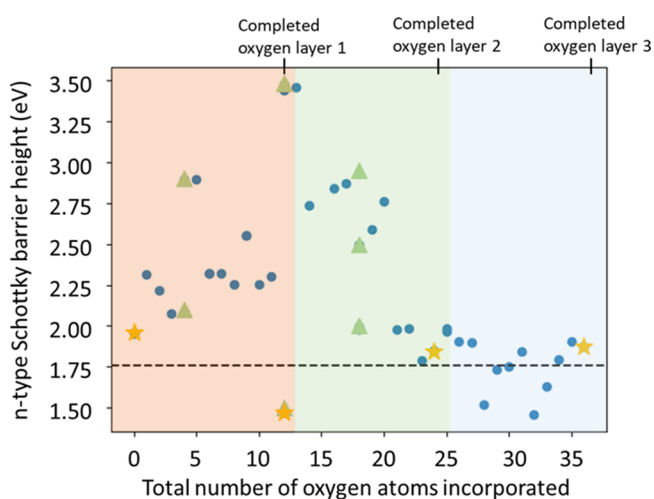


**Figure 8.** Calculated n-SBH for the Al<sub>2</sub>O<sub>3</sub>/Al interface as a function of the total number of oxygen atoms incorporated in three layers of aluminum. Yellow stars denote the n-SBH of the four thermodynamically stable structures shown in Figure 2; the black dotted line indicates their average (1.76 eV). The orange, green, and blue panels denote the regimes where n-SBH increases, decreases, and remains nearly constant, respectively. Note that while the n-SBH shows a correlation with the partial coverage of oxygen per layer, it also depends on the presence of aluminum vacancies. This dependence is shown as green triangles, where the n-SBH value differs at the same total number of oxygen due to the presence of aluminum vacancies in these structures.

the three aluminum layers near the interface. A general trend can be seen, namely, the barrier heights of the four thermodynamically stable configurations discussed in Sections 2.1 and 2.2 are among the lowest (marked as stars),  $\sim 1.76$  eV on average (marked with a dotted line). Furthermore, structures with oxygen coverages less than one layer at the interface tend to increase the n-SBH. Structures with oxygen coverages greater than one layer but less than two layers start to decrease the n-SBH (but the barrier heights are still greater than the thermodynamically stable structures). Finally, those with oxygen coverages greater than two layers but less than three layers do not increase the n-SBH. As discussed in Section 2.2 and Supporting Information Note S3, the thermodynamically stable configurations 1 and 2 have on average  $\sim 1$  e excess per interfacial oxide Al atom, and interfacial oxide Al atoms are completely oxidized to Al<sup>3+</sup> in configurations 3 and 4. In contrast, interfacial Al atoms in structures with partial oxygen coverages  $< 1$  layer tend to have partial charges up to  $\sim 2.2$  e. Such partial charges possibly lead to an increase in n-SBH by increasing the negative charge density at the interface as compared to the thermodynamically stable configurations. The decrease in n-SBH beyond one layer oxygen incorporation at the interface could be due to a decrease in the excess partial charge on interfacial Al atoms as the Al layers near the interface oxidize. Interfacial Al atoms have partial charges up to  $\sim 1.5$  e in structures where oxygen begins to incorporate in the second and third layer, with multiple aluminum atoms being completely oxidized to Al<sup>3+</sup> as the third layer of oxygen is incorporated. This decrease in the excess charge could lead to the observed reduction in barrier heights as the interface aluminum layers oxidize. Note that while Figure 8 shows plots of n-SBH as a function of the total number of oxygen atoms, the n-SBH depends on the number of aluminum atoms at the interface as well. This dependence can be seen from the n-SBH values at 4, 12, and 18 oxygen atoms, which show different values at the same total number of oxygen (marked as triangles). Examination of the structures show that the structures with aluminum vacancies have larger n-SBH (at same number of oxygen atoms, see Supporting Information Note S6), again highlighting the effect of negative charges (aluminum vacancies are acceptors) on n-SBH. It must be mentioned that our use of GGA–PBE likely leads to inaccurate absolute values of the calculated n-SBH due to the underestimation of the Al<sub>2</sub>O<sub>3</sub> band gap. However, the trend of n-SBH dependence on oxygen incorporation (and therefore, dependence on excess charge on under-coordinated interfacial Al atoms) is unaffected by these inaccuracies. In fact, despite DFT-related potential inaccuracies, our calculated n-SBH matches the values measured in the literature, which range from 0.9 to 3.2 eV.<sup>43–49</sup>

Thus, for the Al<sub>2</sub>O<sub>3</sub>/Al interface, a possible mechanism behind the “interface dipole” that screens out the effect of the metal<sup>42</sup> could be the incomplete oxygen incorporation at the interface. This leads to under-coordinated Al cations which alter the SBH.

**2.5. Effect of the Coordination Environment on Interface Core Level Shifts.** Angle-resolved XPS (AR-XPS) experiments on Al<sub>2</sub>O<sub>3</sub> grown on Al via thermal oxidation have revealed that the Al 2p spectra consist of three components, assigned to Al contributions from the bulk metal, deficiently coordinated Al cations at the interface, and Al contributions from the bulk oxide film.<sup>17,18</sup> The study also found the O 1s spectra to constitute three peaks, assigned to O

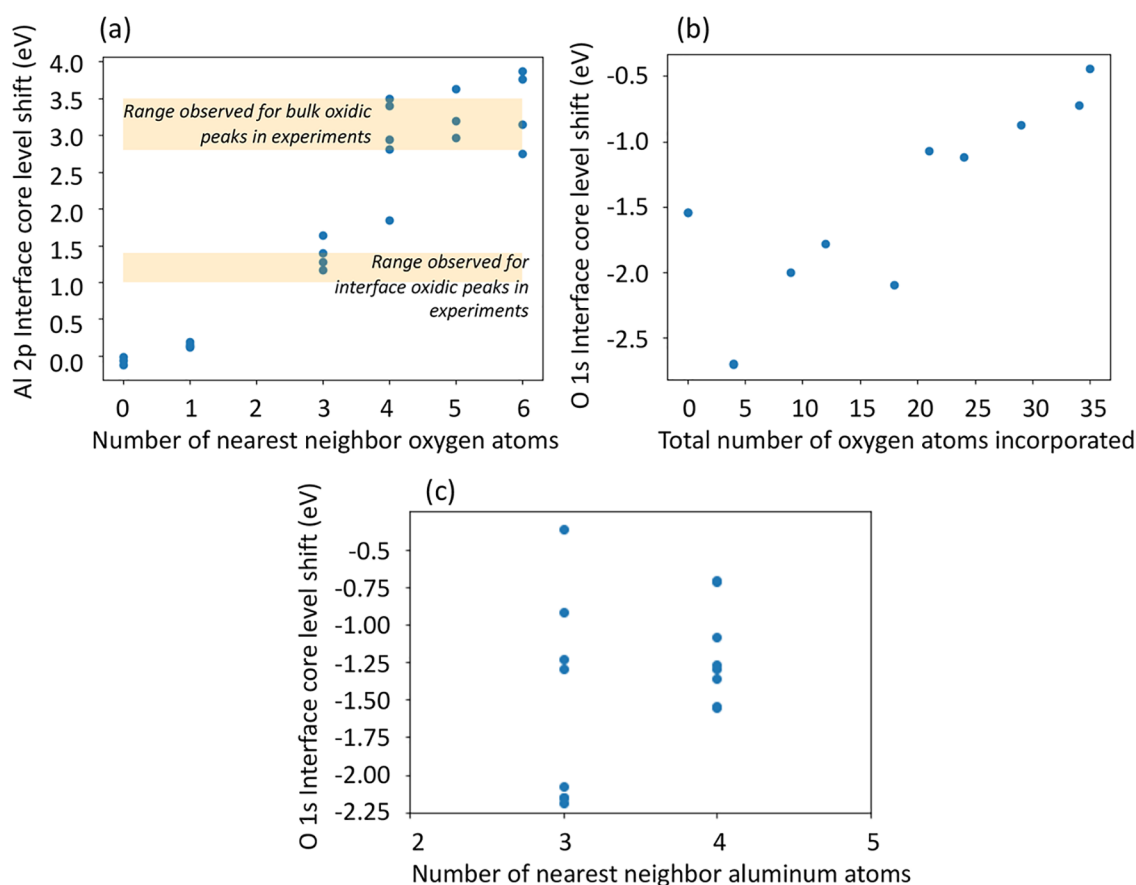


**Figure 9.** ICLS for (a) Al 2p as a function of the number of nearest neighbor O, (b) O 1s as a function of the total number of O incorporated, and (c) O 1s as a function of the number of nearest neighbor Al.

contributions from the interface, bulk oxide, and oxide surface.<sup>17</sup> However, the exact composition and structural features that give rise to these shifts at the interface is still unknown. We therefore computed the Al 2p and O 1s interfacial core-level shifts (ICLS) using the final state approximation method<sup>50</sup> to provide more insights into the interfacial bonding features that give rise to the experimentally observed shifts.

In Figure 9a, we plot the ICLS of Al 2p as a function of the number of nearest neighbor oxygen atoms to the selected aluminum atom. Interfacial aluminum atoms with different numbers of nearest neighbor oxygen were selected from the four thermodynamically stable configurations (see Supporting Information Note S7), and their ICLS was computed. We also mark the range of Al 2p ICLS values measured from experiments at the Al<sub>2</sub>O<sub>3</sub>/Al interface and in bulk oxide grown on Al. From this plot, we see that the ICLS for Al atoms with three nearest neighbor oxygen matches the shift seen for the Al 2p interface component in experiments (~1.5 eV higher than bulk metal). Thus, this analysis reveals that the experimental interfaces that report under-coordinated aluminum at the interface likely consist of aluminum coordinated with three oxygen atoms. Since configurations 1 and 2 in Figure 2a,b have interfacial aluminum atoms primarily coordinated with three oxygen atoms, this indicates that similar structures are likely present at the experimental interfaces formed upon oxidizing Al. We also see that the ICLS for aluminum atoms with 4–5 nearest neighbor oxygen matches the shift seen for the Al 2p bulk oxide component

from experiments. This is reasonable as the experiments likely grow amorphous or  $\gamma$ -Al<sub>2</sub>O<sub>3</sub>, which primarily consist of 4 and 5 coordinated Al atoms.

In Figure 9b, we plot the ICLS of O 1s as a function of the total number of oxygen incorporated in three layers of aluminum. We see that as the number of oxygen incorporated increases and the Al layers near the interface oxidize to form Al<sub>2</sub>O<sub>3</sub>, the O 1s ICLS also gradually shifts to ~0, matching O 1s binding energies in bulk Al<sub>2</sub>O<sub>3</sub>. At lower numbers of oxygen incorporation, we note an ICLS of ~-2 eV, similar to that of experimentally observed O 1s interfacial core-level shifts. Thus, this also points toward experimental interfaces having structures similar to configurations 1 and 2, which have not yet oxidized completely to form bulk Al<sub>2</sub>O<sub>3</sub>.

In Figure 9c, we plot the ICLS of O 1s as a function of the number of nearest neighbor Al. Similar to Figure 9a, interfacial O atoms with different numbers of nearest neighbor Al were selected from the four thermodynamically stable configurations (see Supporting Information Note S7), and their ICLS was computed. In our thermodynamically stable configurations, O was found to exist coordinated with either three or four Al atoms. However, we do not see any clear dependence of ICLS values on the coordination environment of O. Thus, from Figure 9b,c, it is possible that the O 1s ICLS depends on the long-range order (rather than its immediate coordination environment). This could also be the reason why we observe a shift toward ICLS ~0 eV as more oxygen is incorporated (in Figure 9b) due to the formation of bulk oxide.

### 3. DISCUSSION

We use this section to discuss the implications of our study, in the context of providing insights into experimental observations and furthering our understanding of the atomic and electronic structure and propagation of this fundamental interface. We also discuss the broader impact of our findings on the different technological applications of this interface. We end with a comparison of our GCMC-derived interfaces with the models frequently utilized in the *ab initio* literature and a brief examination of the approximations made in this study and their potential effect on the results.

By performing GCMC over a range of realistic  $\mu_{\text{O}}$  at 800 K, we were able to simulate the oxidation of several layers of Al metal near the  $\text{Al}_2\text{O}_3/\text{Al}$  interface. As discussed in Section 2.1, the stable interfaces formed as the oxide propagates are always atomically sharp, interfacial advancement occurs in a layer-by-layer fashion, oxygen incorporates into the next layer of aluminum only after saturating the previous layer and does not penetrate into the metal ahead of the interface front, and the interfacial aluminum plane at the oxide side is always Al-rich. Our study reveals the atomic and electronic structure of the interface as it propagates, including the preferred sites and layer-wise saturation concentrations of oxygen and aluminum as the interface advances. Importantly, our study also reveals that incorporation of oxygen at the interface immediately begins to change the electronic structure of the interfacial Al metal layer, localizing the Al 3s and 3p states and reducing the density of states near the Fermi level. In fact, this depletion of states near the Fermi level and the specific (octahedral) orientation and localization of the excess Al 3sp charge density from under-coordinated interfacial Al cations likely promote the layer-wise propagation of oxygen layers and prevent the dissolution of oxygen ahead of the interface front. This is in sharp contrast to the  $\text{ZrO}_2/\text{Zr}$ <sup>19,20,51</sup> interface, which is known to form interfacial sub-oxides. Unlike Al, oxygen addition to Zr does not change the density of states at the Fermi level,<sup>52</sup> which could be the reason behind the high oxygen solubility in Zr ahead of the  $\text{ZrO}_2/\text{Zr}$  interface front, leading to the formation of interfacial sub-oxides.<sup>52</sup> The changes in the interfacial electronic structure also explain the high corrosion resistance and self-healing nature of the  $\text{Al}_2\text{O}_3/\text{Al}$  system: addition of oxygen to the interface immediately begins to create a band gap within the first layer of Al metal, thus reducing the electron density and preventing electron transfer necessary for scale/metal reactions.<sup>7</sup> By providing atomistic and electronic insights, our findings go beyond previous experimental<sup>14,15</sup> and classical MD<sup>31</sup> studies of  $\text{Al}_2\text{O}_3$  growth on Al (111) via thermal oxidation, which also observe a sharp interface<sup>14,15</sup> and a layer-by-layer growth of the oxide into the metal<sup>31</sup> but do not resolve the explicit atomic and electronic structure of the interface. It is interesting to note that MD studies of  $\text{Al}_2\text{O}_3$  growth on Al (which simulate the kinetics of oxide growth on Al) report layer-by-layer growth of  $\text{Al}_2\text{O}_3$  into Al,<sup>31</sup> similar to our thermodynamically stable structures. This shows the close relationship between thermodynamics and kinetics of this process.

In Section 2.2, we discussed the local events that lead to interfacial advancement and  $\text{Al}_2\text{O}_3$  formation at the interface, namely, oxygen incorporation  $\rightarrow$  aluminum vacancy formation in the interfacial metal plane  $\rightarrow$  further oxygen incorporation  $\rightarrow$  addition of aluminum back to the interstitial sites of the aluminum-deficient plane (i.e., vacancy annihilation)  $\rightarrow$

oxygen incorporation in the next layer, and so forth. Experimental studies<sup>35</sup> propose that  $\text{Al}_2\text{O}_3$  growth occurs both at air/ $\text{Al}_2\text{O}_3$  and  $\text{Al}_2\text{O}_3/\text{metal}$  interfaces via a counter-current grain boundary diffusion of aluminum toward the air/ $\text{Al}_2\text{O}_3$  interface and oxygen toward the  $\text{Al}_2\text{O}_3/\text{metal}$  interface (but the latter is predominant). Annihilation of the resulting interfacial aluminum vacancy is hypothesized to occur via vacancy injection into the Al metal reservoir.<sup>36,53</sup> While the scale/metal reactions have only been indirectly inferred in prior experiments and phenomenological models, our study explicitly reveals the reactions at the scale/metal interface that lead to the formation of  $\text{Al}_2\text{O}_3$  by focusing on the  $\text{Al}_2\text{O}_3/\text{Al}$  interface during oxide growth and by incorporating three oxygen layers. Moreover, by inserting and removing aluminum and oxygen in the GCMC simulation, this study uniquely provides insights into the structures that could arise from the counter-diffusion mechanism of  $\text{Al}_2\text{O}_3$  growth.

Our findings also provide additional insights into the experimental observations related to the electronic properties of the  $\text{Al}_2\text{O}_3/\text{Al}$  interface. In particular, multiple experiments<sup>16,45,54,55</sup> postulate Al excess near the interface region (up to depths of  $\sim 4$  nm into the oxide<sup>16,54</sup>), which is hypothesized to be a positive space charge region, based on Al–O chemical and binding state analyses,<sup>16,54</sup> electron force microscopy measurements,<sup>55</sup> and tunneling current vs voltage analysis.<sup>45</sup> Our study provides insights into a potential reason behind the positive space charge region: as discussed in Section 2.3, the interfacial mid-gap states (of configurations 1 and 2, which likely form at equilibrium) accommodate the excess negative charge density from under-coordinated interfacial Al atoms from  $\text{Al}_2\text{O}_3$ . Thus, when this interfacial negative charge density becomes sufficiently high, it can result in the formation of a positive space charge region, as observed in experiments. Additionally, experimental measurements of SBHs at  $\text{Al}_2\text{O}_3/\text{Al}$  interfaces report a wide range of n-SBH values, ranging from 0.76 to 3.2 eV.<sup>43–49</sup> Our findings in Section 2.4 indicate a possible reason behind the experimental scattering, thus providing a strategy to control the n-SBH. We show that the calculated n-SBH depends strongly on the interface composition: interfaces with partial O coverages per layer (i.e., reduced interfaces) display increased n-SBH. Thus, the n-SBH can be engineered by altering the  $\text{Al}_2\text{O}_3$  growth or Al deposition environments (e.g., changing surface preparation, annealing conditions, etc.). In fact, comparison of oxidizing environments in different experimental studies shows that there may be a tendency for stronger oxidizing environments,<sup>45,47,48</sup> resulting in lower n-SBH. Finally, our findings in Section 2.5 reveal that three-coordinated Al atoms at the interface are the reason behind the higher binding energies of the interfacial Al 2p peaks,<sup>17</sup> and the lower binding energies of interfacial O 1s peaks could be due to the lack of the long-range order at the interface before it oxidizes to form  $\text{Al}_2\text{O}_3$ . This provides new perspectives into analyzing XPS data of this interface.

It is relevant to discuss the implications of the computed atomic and electronic properties of the  $\text{Al}_2\text{O}_3/\text{Al}$  interface on the performance of electronic devices and corrosion barriers.  $\text{Al}_2\text{O}_3$  is used as a gate dielectric and capping layer in MOS technology,<sup>5,56,57</sup> where the metal/ $\text{Al}_2\text{O}_3$  interface plays an important role in determining the threshold voltage and drive current by altering the effective work function of the gate metal. At high densities, the occupied interfacial mid-gap states reported in our study can pin the Fermi level, thereby making

the effective work function independent of the metal. This can prevent the favorable tuning of the device performance of Al<sub>2</sub>O<sub>3</sub>-based microelectronics. The presence of occupied interfacial mid-gap states can also give rise to flux noise in superconducting qubits,<sup>40</sup> limiting their coherence time and preventing their scale-up. By revealing the nature of these mid-gap states and their dependence on the interfacial composition, this study can aid in engineering of the interface to reduce the contribution of these states to qubit decoherence. On the other hand, the interface also has a finite density of unoccupied mid-gap states. These states can accommodate excess electrons and can alter the defect formation energy, as has been computed for oxygen vacancy formation at TiO<sub>2</sub>/Pt<sup>58,59</sup> and CeO<sub>2</sub>/Pd<sup>60</sup> interfaces. The presence of unoccupied mid-gap states can thus aid in the preferential formation of defects like hydrogen interstitials and oxygen vacancies at the Al<sub>2</sub>O<sub>3</sub>/Al interface, which can form two-level systems and contribute to decoherence in superconducting qubits.<sup>10,11,61</sup> Changes to the interfacial composition can also change the SBH, which have consequences for qubit and tunnel junction applications. In the context of barrier coatings, interfacial defect segregation can prevent scale/metal reactions.<sup>53</sup> As revealed by the GCMC trajectory, such reactions (such as aluminum vacancy formation and annihilation) are crucial building blocks for interface propagation, whose inhibition can retard protective scale growth.<sup>53</sup> Charged defect segregation to the interface has important implications for the use of Al<sub>2</sub>O<sub>3</sub> as a corrosion barrier as well since this can alter the space charge layer, thereby altering the corrosion resistance performance. Our study reveals that depletion of metallic states near the Fermi level upon oxygen incorporation may be key to designing self-healing corrosion-resistant coatings. Thus, the profound effects of occupied and unoccupied interfacial mid-gap states on the properties of microelectronics and barrier coatings employing Al<sub>2</sub>O<sub>3</sub>/Al provide a route to engineer the performance of these systems.

Note that apart from some structural and electronic similarities, none of the four thermodynamically stable structures correspond to the interfacial structures commonly reported for the Al<sub>2</sub>O<sub>3</sub>/Al interface in the ab initio literature.<sup>21–23</sup> This indicates that the idealized interfaces frequently used in DFT analyses of interfacial work of adhesion, electronic structure, bonding character, and so forth are likely metastable. It is worthwhile to add here that the structure labeled configuration 1 in Figure 2, with 12.5% V<sub>Al</sub> at the interface, corresponds well with the AIMD study of the Al<sub>2</sub>O<sub>3</sub>/liquid Al interface.<sup>62</sup> The latter study has also found that the interface favors ~10% V<sub>Al</sub> at Al<sub>2</sub>O<sub>3</sub>–Al equilibrium. Our ab initio GCMC simulation was able to find this favorable structure entirely on its own, underscoring the unbiased and exhaustive exploration performed by this simulation.

We end this section with a discussion on the approximations made in our study and their possible influence on the results:

- (a) We model the coherent interface between  $\alpha$ -Al<sub>2</sub>O<sub>3</sub> and Al by fixing the in-plane  $\alpha$ -Al<sub>2</sub>O<sub>3</sub>(0001) lattice parameters to match that of Al(111). This mimics Al<sub>2</sub>O<sub>3</sub> growth on Al and reflects experimental findings that show that Al<sub>2</sub>O<sub>3</sub> grows epitaxially on Al(111) as the latter is oxidized.<sup>15,63</sup> The misfit strain is ~3%, so this interface will likely have large regions of coherence between misfit dislocations. While this strain configuration was opted to match experimental data, we note

that GCMC explores only that region of the potential energy landscape where  $\alpha$ -Al<sub>2</sub>O<sub>3</sub>(0001) is strained in-plane to match Al(111) lattice parameters. This limitation could influence our results. However, since other computational studies of Al(111) surface oxidation<sup>31</sup> and those utilizing Al<sub>2</sub>O<sub>3</sub> lattice parameters while modeling the Al<sub>2</sub>O<sub>3</sub>/Al<sup>62</sup> interface also show similar layer-wise oxide propagation<sup>31,62</sup> and Al vacancy concentrations at the interface,<sup>62</sup> we do not expect the strain constraint to significantly influence our results.

- (b) We do not include vibrational or electronic entropic effects in our calculations, except for the temperature dependence of  $\mu_{\text{O}}$  and  $\mu_{\text{Al}}$ , which we take from the NIST-JANAF tables.<sup>64</sup> However, since the GCMC acceptance probability criteria are based on relative energies of the different configurations, and since we are dealing with solids, it is likely that the vibrational contributions will cancel out, and the contribution of electronic entropy is small. Thus, excluding vibrational and electronic entropic effects is not expected to alter our results.
- (c) Finally, the interface system that we have chosen to simulate is  $\alpha$ -Al<sub>2</sub>O<sub>3</sub>/Al. While  $\alpha$ -Al<sub>2</sub>O<sub>3</sub> is the thermodynamically stable phase at thicknesses above ~1 nm on Al,<sup>15,23</sup> experiments primarily observe only amorphous or metastable  $\gamma$ -Al<sub>2</sub>O<sub>3</sub> grown on Al. This is because the kinetic barriers to transform the metastable  $\gamma$ -Al<sub>2</sub>O<sub>3</sub> or other metastable phases of Al<sub>2</sub>O<sub>3</sub> to  $\alpha$ -Al<sub>2</sub>O<sub>3</sub> are high<sup>65</sup> (~5 eV). However, since our focus in this work was to use GCMC to evaluate thermodynamically stable interfacial configurations, it was more reasonable to build the interface with  $\alpha$ -Al<sub>2</sub>O<sub>3</sub>. Since our results indicate that the interface propagation mechanism (layer-by-layer, with O incorporation, V<sub>Al</sub> formation, V<sub>Al</sub> annihilation, etc.) and the interfacial electronic properties depend largely on the local interfacial interactions (and not on the phase of the Al<sub>2</sub>O<sub>3</sub> above), the findings could still be applicable to studies which deposit  $\alpha$ -Al<sub>2</sub>O<sub>3</sub> on Al (or vice versa) and those that grow different phases of Al<sub>2</sub>O<sub>3</sub> via Al oxidation. However, the high computational cost of ab initio simulations admittedly did limit our GCMC study to only a single phase of Al<sub>2</sub>O<sub>3</sub> and a single interface orientation, with fixed lattice parameters. In the future, utilizing machine-learning force fields to calculate the energies of the configurations generated by GCMC (at ab initio accuracy) might enable us to explore multiple phases of Al<sub>2</sub>O<sub>3</sub> and multiple interface orientations and strain conditions, with larger number of GCMC moves and larger supercell sizes.

## 4. CONCLUSIONS

By performing a physically motivated and unbiased exploration of the interface composition and configuration space using ab initio GCMC, this study addresses multiple open questions related to the equilibrium structure of the Al<sub>2</sub>O<sub>3</sub>/Al interface, concentrations of Al and O and their preferential positions at the interface, and the evolution of the structural and electronic properties during the initial stages of interface propagation into the metal. We identified that the interface is atomically sharp and contains 12.5% aluminum vacancies at the oxide side at equilibrium. As  $\Delta\mu_{\text{O}}$  is slightly increased, interface propagation

occurs in a layer-by-layer fashion, and the interfacial Al plane at the oxide side is always Al-rich. Even as it advances, the interface is always atomically sharp, and oxygen incorporation in the subsequent metal layer occurs only after saturation of the previous layer. By analyzing the GCMC trajectory, we identified oxygen incorporation, aluminum vacancy formation, and aluminum vacancy annihilation to be the local events at the interface that lead to Al<sub>2</sub>O<sub>3</sub> formation. Analysis of the electronic structure revealed that under-coordinated interfacial Al atoms at the oxide side strongly contribute to the interfacial mid-gap states, and the incorporation of oxygen at the interface immediately causes the localization and depletion of Al states near the Fermi level. This prevents oxygen dissolution ahead of the interface front and results in the layer-by-layer propagation of the interface and also explains the important self-healing nature of the Al<sub>2</sub>O<sub>3</sub>/Al system. This is in contrast to the ZrO<sub>2</sub>/Zr system which forms interfacial sub-oxides. Metal-induced gap states have a minor contribution but likely stabilize the excess Al interstitials at the interfacial oxide plane. Furthermore, the computed n-type SBHs were found to be strongly dependent on the interfacial composition, and the calculated interfacial Al 2p and O 1s core-level shifts were found to be linearly dependent on the Al coordination and long-range order, respectively. These findings have important implications for the design of Al<sub>2</sub>O<sub>3</sub>/Al-based applications such as protective coatings, transistor technologies, and superconducting qubits, where the atomic and electronic structure of the oxide/metal interface affects properties such as corrosion resistance, threshold voltages, and coherence times.

## 5. COMPUTATIONAL METHODS

We use ab initio GCMC to identify the equilibrium interfacial configuration at a fixed volume, temperature, and oxygen and aluminum chemical potentials. The theory behind GCMC is described in detail in previous studies;<sup>32,66–68</sup> therefore, we summarize only the main points here. We sample the configuration space via two moves: insertion of an Al or O atom (with equal probability) into the interface region and removal of an Al or O atom from the interface region. Translation moves did not improve the acceptance ratio and therefore were not used to sample the phase space. After every trial move, we relax the configuration and compute the energy using DFT. The acceptance probabilities are given as

$$P_{\text{insert}} = \min \left[ 1, \frac{V}{\Lambda^3(N+1)} e^{-(U_2 - U_1 - \mu)/k_B T} \right] \quad (1)$$

$$P_{\text{remove}} = \min \left[ 1, \frac{N\Lambda^3}{V} e^{-(U_2 - U_1 + \mu)/k_B T} \right] \quad (2)$$

where  $V$  is the volume of the system,  $\Lambda$  is the thermal de Broglie wavelength of the inserted/removed atom (given by  $\Lambda = \frac{h}{\sqrt{2\pi m k_B T}}$ ,  $h$  is the Planck constant,  $m$  is the mass of the atom,  $k_B$  is the Boltzmann constant, and  $T$  is the temperature of the reservoir),  $N$  is the number of atoms of the type being inserted/removed,  $U_1$  and  $U_2$  are the potential energies of the relaxed configurations before and after the GCMC move, respectively, calculated using DFT, and  $\mu$  is the chemical potential of the reservoir from which insertion/removal is performed.

The relaxation step is necessary to allow for rearrangement of the interface and lowering of the potential energy of the configuration; however, it introduces a bias that disturbs detailed balance.<sup>67,68</sup> We therefore replace the system volume  $V$  in the acceptance probabilities with an “accessible volume”  $V_{\text{acc}}$  to counter this bias, given as  $V_{\text{acc}} = V - N_{\text{Al}}4/3\pi r_{\text{Al}}^3 - N_{\text{O}}4/3\pi r_{\text{O}}^3$ , as discussed in previous studies,<sup>67,68</sup> where  $N_{\text{Al}}$  and  $N_{\text{O}}$  are the number of Al and O atoms in the interface

region, respectively, and  $r_{\text{Al}}$  and  $r_{\text{O}}$  are their respective atomic radii ( $r_{\text{Al}} = 1.402 \text{ \AA}$  and  $r_{\text{O}} = 0.9 \text{ \AA}$ , taken from the Wigner–Seitz radii reported in the VASP<sup>69–71</sup> POTCAR files for the respective elements). To ensure relevant and efficient sampling of interfacial configurations, we constrain the insertion/removal of the atoms to the interfacial region, as described below. We also include a configurational bias to prevent the inserted atom from being too close (1 Å) to its nearest atom. These constraints do not affect the detailed balance as the configurations eliminated by these constraints likely have high energies and would not have been accepted. GCMC moves are performed until the system energy converges. Ultimately, through this scheme, we generate a large number of interface structures relevant to the temperature and chemical potential of interest.

Our interface model is shown in Figure 1a. The starting structure was obtained upon relaxing O-terminated  $\alpha$ -Al<sub>2</sub>O<sub>3</sub> (0001) (with 6 O layers,  $\sim 11 \text{ \AA}$ ) on Al (111) (with 7 Al layers,  $\sim 14 \text{ \AA}$ ) in FCC stacking with a periodic interface arrangement. This idealized interface matches the close-packed planes and directions of Al<sub>2</sub>O<sub>3</sub> and Al (i.e.,  $(111)_{\text{Al}} \parallel (0001)_{\text{Al}_2\text{O}_3}$  and  $\langle \bar{1}01 \rangle_{\text{Al}} \parallel \langle 01\bar{1}0 \rangle_{\text{Al}_2\text{O}_3}$ ,  $\langle \bar{1}2\bar{1} \rangle_{\text{Al}} \parallel \langle 2\bar{1}\bar{1}0 \rangle_{\text{Al}_2\text{O}_3}$ ), which has been reported in experiments of Al<sub>2</sub>O<sub>3</sub> grown on Al<sup>15</sup> and Al deposited on sapphire<sup>72,73</sup> and is reported to be the most stable across a wide range of  $\mu_{\text{O}}$ .<sup>21,22,24</sup> To mimic epitaxial growth of Al<sub>2</sub>O<sub>3</sub> on Al, as observed during thermal oxidation of Al,<sup>15,63</sup> Al<sub>2</sub>O<sub>3</sub> (0001) is strained in-plane to match Al (111). To obtain the starting interface structure, the cell was allowed to relax along the  $c$ -axis, keeping the  $a$ - and  $b$ -lattice parameters fixed. For the GCMC calculations, the supercell lattice parameters are fixed, and atoms in the interface region are relaxed, with the layers farther away from the interface (including the opposite interface) fixed to mimic the oxide and metal bulk, as shown in Figure 1a.

We perform the GCMC simulation at 800 K (to ensure reasonable acceptance ratio and to reflect common Al oxidation conditions<sup>15,16</sup>), over a range of  $\mu_{\text{O}}$  near the equilibrium between bulk Al<sub>2</sub>O<sub>3</sub>(s) and bulk Al(s). The chemical potentials are calculated as

$$\mu_{\text{Al}} = \mu_{\text{Al}}^{\text{eq}} = E_{\text{Al}}^{\text{DFT}} + \Delta\mu_{\text{Al}}(T) \quad (3)$$

$$\mu_{\text{Al}_2\text{O}_3} = \mu_{\text{Al}_2\text{O}_3}^{\text{eq}} = E_{\text{Al}_2\text{O}_3}^{\text{DFT}} + \Delta\mu_{\text{Al}_2\text{O}_3}(T) \quad (4)$$

$$\mu_{\text{O}}^{\text{eq}} = \frac{\mu_{\text{Al}_2\text{O}_3}^{\text{eq}} - 2\mu_{\text{Al}}^{\text{eq}}}{3} \quad (5)$$

where the temperature-dependent terms are obtained from NIST-JANAF tables.<sup>64</sup> Starting from the idealized interface, atom insertion/removal is performed in the interface region, as described above.  $\mu_{\text{Al}}$  is fixed to that of the metal ( $\mu_{\text{Al}} = \mu_{\text{Al}}^{\text{eq}}$ ), and  $\mu_{\text{O}}$  is slightly increased ( $\Delta\mu_{\text{O}} = \mu_{\text{O}} - \mu_{\text{O}}^{\text{eq}}$ ) to reflect the increase in the concentration as oxygen is incorporated at the interface, and the interface propagates. This also enables the sampling of a variety of interfacial structures and compositions. We tested eight different  $\Delta\mu_{\text{O}}$  (0.0–0.35 eV in steps of 0.05 eV). The relative interface formation energies of the various configurations explored by GCMC were calculated as

$$E_{\text{relative}} = E_{\text{system}} - (E_{\text{ref}} + \Delta N_{\text{Al}}\mu_{\text{Al}} + \Delta N_{\text{O}}\mu_{\text{O}}) \quad (6)$$

where  $E_{\text{system}}$  is the total DFT energy of the configuration,  $E_{\text{ref}}$  is the reference DFT energy of the idealized interface, as shown in Figure 1a,  $\Delta N_{\text{Al}}$  is the number of Al atoms relative to the idealized interface, and  $\Delta N_{\text{O}}$  is the number of O atoms relative to the idealized interface. Thus, since  $E_{\text{ref}}$  is identical for all interface configurations, this formalism enables the comparison of the relative stabilities of the different interfaces explored by GCMC.

LAMMPS<sup>74</sup> was used to carry out the GCMC moves, and VASP v. 5.4.3<sup>69–71</sup> was used to calculate the energies of each structure generated by GCMC. Further details about the DFT calculation settings are provided in Supporting Information Note S1.

The SBH for different interfacial structures were calculated using the core-level alignment method.<sup>75,76</sup> In this method, the p-type SBH ( $\phi_p$ ) is calculated as the difference between the Fermi level of the system ( $\epsilon_{F,\text{sys}}$ ) and the valence band maximum of the bulk oxide

( $\epsilon_{\text{VBM,oxide}}$ ). The deep O 1s core-level energy of an O atom [far from the interface for the  $\text{Al}_2\text{O}_3/\text{Al}$  system ( $\epsilon_{\text{O1s,sys}}$ ) and in the  $\text{Al}_2\text{O}_3$  bulk ( $\epsilon_{\text{O1s,oxide}}$ ), respectively] is chosen as the reference level to align the system Fermi level and the oxide VBM. A schematic band diagram describing this method is given in Supporting Information Note S6.

$$\phi_{\text{p}} = [\epsilon_{\text{F,sys}} - \epsilon_{\text{O1s,sys}}] - [\epsilon_{\text{VBM,oxide}} - \epsilon_{\text{O1s,oxide}}] \quad (7)$$

In the above formalism, the O 1s core-level energies are calculated in the initial state approximation<sup>50</sup> with an  $8 \times 8 \times 3$  k-mesh. The n-SBH ( $\phi_{\text{n}}$ ) is then calculated as the difference between the band gap of the oxide ( $E_{\text{g}}$ , calculated to be 5.84 eV) and the p-type SBH

$$\phi_{\text{n}} = E_{\text{g}} - \phi_{\text{p}} \quad (8)$$

Al 2p and O 1s interface core-level binding energy shifts were calculated using the final state approximation<sup>50</sup> with an  $8 \times 8 \times 3$  k-mesh. The Al 2p core-level shifts for interface Al atoms were determined relative to a reference bulk Al atom from a separate bulk calculation. Similarly, O 2p core-level shifts for interface O atoms were determined relative to a reference O atom in bulk  $\text{Al}_2\text{O}_3$  from a separate bulk calculation.

## ■ ASSOCIATED CONTENT

### SI Supporting Information

The Supporting Information is available free of charge at <https://pubs.acs.org/doi/10.1021/acsami.2c08706>.

Additional computational methods and details, including DFT calculation setup, Bader charges, and ab initio molecular dynamics analysis (PDF)

## ■ AUTHOR INFORMATION

### Corresponding Author

**Bilge Yildiz** – Department of Materials Science and Engineering, Massachusetts Institute of Technology, Cambridge, Massachusetts 02139, United States; Department of Nuclear Science and Engineering, Massachusetts Institute of Technology, Cambridge, Massachusetts 02139, United States; [orcid.org/0000-0002-2688-5666](https://orcid.org/0000-0002-2688-5666); Phone: 617-324-4009; Email: [byildiz@mit.edu](mailto:byildiz@mit.edu)

### Author

**Vrinda Somjit** – Department of Materials Science and Engineering, Massachusetts Institute of Technology, Cambridge, Massachusetts 02139, United States; [orcid.org/0000-0002-8396-2904](https://orcid.org/0000-0002-8396-2904)

Complete contact information is available at: <https://pubs.acs.org/10.1021/acsami.2c08706>

### Author Contributions

V.S. contributed the code and performed the simulations. B.Y. supervised the work. Both authors discussed the results and wrote the manuscript.

### Notes

The authors declare no competing financial interest. Further information and requests for data and code will be made available by the corresponding author, B.Y. ([byildiz@mit.edu](mailto:byildiz@mit.edu)).

## ■ ACKNOWLEDGMENTS

We are grateful to Prof. Ju Li for providing insightful comments and feedback regarding the simulations. We also thank Dr. Konstantin Klyukin and Dr. Pjotr Zguns for helpful discussion. This work was supported by Exelon Corporation

and MIT Energy Initiative Graduate Student Fellowship. This work used the Extreme Science and Engineering Discovery Environment (XSEDE) resources Stampede2 at the Texas Advanced Computing Center (TACC) and Expanse at the San Diego Supercomputer Center (SDSC) through allocation number TG-DMR120025. XSEDE is supported by National Science Foundation grant number ACI-1548562. This work also used Frontera at the Texas Advanced Computing Center through allocation number DMR20012. We thank the staff at TACC and SDSC for technical support.

## ■ REFERENCES

- (1) Baudin, C. *Encyclopedia of Materials: Technical Ceramics and Glasses*; Elsevier, 2021.
- (2) Aluminum Statistics and Information. National Minerals Information Center. <https://www.usgs.gov/centers/national-minerals-information-center/aluminum-statistics-and-information> (accessed Mar 1, 2022).
- (3) Yin, Z.; Tao, S.; Zhou, X.; Ding, C. Microstructure and Mechanical Properties of  $\text{Al}_2\text{O}_3$ -Al Composite Coatings Deposited by Plasma Spraying. *Appl. Surf. Sci.* **2008**, *254*, 1636–1643.
- (4) de Leon, N. P.; Itoh, K. M.; Kim, D.; Mehta, K. K.; Northup, T. E.; Paik, H.; Palmer, B.; Samarth, N.; Sangtawesin, S.; Steuerma, D. Materials Challenges and Opportunities for Quantum Computing Hardware. *Science* **2021**, *372*, No. eabb2823.
- (5) Winter, R.; Krylov, I.; Cytermann, C.; Tang, K.; Ahn, J.; McIntyre, P.; Eizenberg, M. Fermi Level Pinning in Metal/ $\text{Al}_2\text{O}_3$ /Ingaas Gate Stack after Post Metallization Annealing. *J. Appl. Phys.* **2015**, *118*, 055302.
- (6) Burgos, N.; Paulis, M.; Mirari Antxustegi, M. M.; Montes, M. Deep Oxidation of Voc Mixtures with Platinum Supported on  $\text{Al}_2\text{O}_3$ /Al Monoliths. *Appl. Catal., B* **2002**, *38*, 251–258.
- (7) Heuer, A.; Nakagawa, T.; Azar, M.; Hovis, D.; Smialek, J.; Gleeson, B.; Hine, N.; Guhl, H.; Lee, H.-S.; Tangney, P.; Foulkes, W. M. C.; Finnis, M. W. On the Growth of  $\text{Al}_2\text{O}_3$  Scales. *Acta Mater.* **2013**, *61*, 6670–6683.
- (8) Wang, X.-G.; Smith, J. R.; Evans, A. Fundamental Influence of C on Adhesion of the a  $\text{L}_2\text{O}_3$ /a L Interface. *Phys. Rev. Lett.* **2002**, *89*, 286102.
- (9) Xie, D.-G.; Wang, Z.-J.; Sun, J.; Li, J.; Ma, E.; Shan, Z.-W. In Situ Study of the Initiation of Hydrogen Bubbles at the Aluminium Metal/Oxide Interface. *Nat. Mater.* **2015**, *14*, 899–903.
- (10) Zeng, L.; Tran, D. T.; Tai, C.-W.; Svensson, G.; Olsson, E. Atomic Structure and Oxygen Deficiency of the Ultrathin Aluminium Oxide Barrier in Al/AlO<sub>x</sub>/Al Josephson Junctions. *Sci. Rep.* **2016**, *6*, 29679.
- (11) Gordon, L.; Abu-Farsakh, H.; Janotti, A.; Van de Walle, C. G. Hydrogen Bonds in  $\text{Al}_2\text{O}_3$  as Dissipative Two-Level Systems in Superconducting Qubits. *Sci. Rep.* **2014**, *4*, 7590.
- (12) Do, Y. H.; Kwak, J. S.; Hong, J. P.; Jung, K.; Im, H. Al Electrode Dependent Transition to Bipolar Resistive Switching Characteristics in Pure  $\text{TiO}_2$  Films. *J. Appl. Phys.* **2008**, *104*, 114512.
- (13) Koberidze, M.; Feshchenko, A.; Puska, M.; Nieminen, R.; Pekola, J. Effect of Interface Geometry on Electron Tunnelling in Al/ $\text{Al}_2\text{O}_3$ /Al Junctions. *J. Phys. D: Appl. Phys.* **2016**, *49*, 165303.
- (14) Nguyen, L.; Hashimoto, T.; Zakharov, D. N.; Stach, E. A.; Rooney, A. P.; Berkels, B.; Thompson, G. E.; Haigh, S. J.; Burnett, T. L. Atomic-Scale Insights into the Oxidation of Aluminum. *ACS Appl. Mater. Interfaces* **2018**, *10*, 2230–2235.
- (15) Jeurgens, L.; Sloof, W.; Tichelaar, F.; Mittemeijer, E. Structure and Morphology of Aluminium-Oxide Films Formed by Thermal Oxidation of Aluminium. *Thin Solid Films* **2002**, *418*, 89–101.
- (16) Jeurgens, L.; Sloof, W.; Tichelaar, F.; Mittemeijer, E. Composition and Chemical State of the Ions of Aluminium-Oxide Films Formed by Thermal Oxidation of Aluminium. *Surf. Sci.* **2002**, *506*, 313–332.

- (17) Reichel, F.; Jeurgens, L.; Richter, G.; Mittemeijer, E. Amorphous Versus Crystalline State for Ultrathin Al<sub>2</sub>O<sub>3</sub> Overgrowths on Al Substrates. *J. Appl. Phys.* **2008**, *103*, 093515.
- (18) Flötotto, D.; Wang, Z.; Mittemeijer, E. J. On the Structural Development During Ultrathin Amorphous Al<sub>2</sub>O<sub>3</sub> Film Growth on Al (111) and Al (100) Surfaces by Thermal Oxidation. *Surf. Sci.* **2015**, *633*, 1–7.
- (19) Motta, A. T.; Yilmazbayhan, A.; Comstock, R. J.; Partezana, J.; Sabol, G. P.; Lai, B.; Cai, Z. *Microstructure and Growth Mechanism of Oxide Layers Formed on Zr Alloys Studied with Micro-Beam Synchrotron Radiation*; ASTM International, 2005.
- (20) Yilmazbayhan, A.; Breval, E.; Motta, A. T.; Comstock, R. J. Transmission Electron Microscopy Examination of Oxide Layers Formed on Zr Alloys. *J. Nucl. Mater.* **2006**, *349*, 265–281.
- (21) Siegel, D. J.; Hector, L. G., Jr.; Adams, J. B. Adhesion, Atomic Structure, and Bonding at the Al (111)/Al–Al<sub>2</sub>O<sub>3</sub> (0001) Interface: A First Principles Study. *Phys. Rev. B: Condens. Matter Mater. Phys.* **2002**, *65*, 085415.
- (22) Koberidze, M.; Puska, M.; Nieminen, R. Structural Details of Al/Al<sub>2</sub>O<sub>3</sub> Junctions and Their Role in the Formation of Electron Tunnel Barriers. *Phys. Rev. B* **2018**, *97*, 195406.
- (23) Aykol, M.; Persson, K. A. Oxidation Protection with Amorphous Surface Oxides: Thermodynamic Insights from Ab Initio Simulations on Aluminum. *ACS Appl. Mater. Interfaces* **2018**, *10*, 3039–3045.
- (24) Feng, J.; Zhang, W.; Jiang, W. Ab Initio Study of Ag/Al<sub>2</sub>O<sub>3</sub> and Au/Al<sub>2</sub>O<sub>3</sub> Interfaces. *Phys. Rev. B: Condens. Matter Mater. Phys.* **2005**, *72*, 115423.
- (25) Kim, C.-E.; Ray, K. G.; Lordi, V. A Density-Functional Theory Study of the Al/AlO<sub>x</sub>/Al Tunnel Junction. *J. Appl. Phys.* **2020**, *128*, 155102.
- (26) Lanthony, C.; Ducéré, J. M.; Rouhani, M. D.; Hemeryck, A.; Estève, A.; Rossi, C. On the Early Stage of Aluminum Oxidation: An Extraction Mechanism Via Oxygen Cooperation. *J. Chem. Phys.* **2012**, *137*, 094707.
- (27) Kiejna, A.; Lundqvist, B. I. First-Principles Study of Surface and Subsurface O Structures at Al (111). *Phys. Rev. B: Condens. Matter Mater. Phys.* **2001**, *63*, 085405.
- (28) Jennison, D.; Verdozzi, C.; Schultz, P.; Sears, M. Ab Initio Structural Predictions for Ultrathin Aluminum Oxide Films on Metallic Substrates. *Phys. Rev. B: Condens. Matter Mater. Phys.* **1999**, *59*, R15605.
- (29) Ciacchi, L. C.; Payne, M. C. “Hot-Atom” O<sub>2</sub> Dissociation and Oxide Nucleation on Al (111). *Phys. Rev. Lett.* **2004**, *92*, 176104.
- (30) Cyster, M. J.; Smith, J. S.; Vogt, N.; Opletal, G.; Russo, S. P.; Cole, J. H. Simulating the Fabrication of Aluminum Oxide Tunnel Junctions. *Npj Quantum Inf.* **2021**, *7*, 12.
- (31) Hasnaoui, A.; Politano, O.; Salazar, J.; Aral, G.; Kalia, R.; Nakano, A.; Vashishta, P. Molecular Dynamics Simulations of the Nano-Scale Room-Temperature Oxidation of Aluminum Single Crystals. *Surf. Sci.* **2005**, *579*, 47–57.
- (32) Wexler, R. B.; Qiu, T.; Rappe, A. M. Automatic Prediction of Surface Phase Diagrams Using Ab Initio Grand Canonical Monte Carlo. *J. Phys. Chem. C* **2019**, *123*, 2321–2328.
- (33) Du, J.-P.; Geng, W.-T.; Arakawa, K.; Li, J.; Ogata, S. Hydrogen-Enhanced Vacancy Diffusion in Metals. *J. Phys. Chem. Lett.* **2020**, *11*, 7015–7020.
- (34) Momma, K.; Izumi, F. Vesta 3 for Three-Dimensional Visualization of Crystal, Volumetric and Morphology Data. *J. Appl. Crystallogr.* **2011**, *44*, 1272–1276.
- (35) Tolpygo, V.; Clarke, D. Microstructural Evidence for Counter-Diffusion of Aluminum and Oxygen During the Growth of Alumina Scales. *Mater. High Temp.* **2003**, *20*, 261–271.
- (36) Hirth, J. P.; Pieraggi, B.; Rapp, R. A. The Role of Interface Dislocations and Ledges as Sources/Sinks for Point Defects in Scaling Reactions. *Acta Metall. Mater.* **1995**, *43*, 1065–1073.
- (37) Finnis, M.; Lozovoi, A.; Alavi, A. The Oxidation of NiAl: What Can We Learn from Ab Initio Calculations? *Annu. Rev. Mater. Res.* **2005**, *35*, 167–207.
- (38) Lee, C.-K.; Cho, E.; Lee, H.-S.; Seol, K. S.; Han, S. Comparative Study of Electronic Structures and Dielectric Properties of Alumina Polymorphs by First-Principles Methods. *Phys. Rev. B: Condens. Matter Mater. Phys.* **2007**, *76*, 245110.
- (39) Perdew, J. P.; Burke, K.; Ernzerhof, M. Generalized Gradient Approximation Made Simple. *Phys. Rev. Lett.* **1996**, *77*, 3865.
- (40) Choi, S.; Lee, D.-H.; Louie, S. G.; Clarke, J. Localization of Metal-Induced Gap States at the Metal-Insulator Interface: Origin of Flux Noise in Squids and Superconducting Qubits. *Phys. Rev. Lett.* **2009**, *103*, 197001.
- (41) Bardeen, J. Surface States and Rectification at a Metal Semiconductor Contact. *Phys. Rev.* **1947**, *71*, 717.
- (42) Tung, R. T. The Physics and Chemistry of the Schottky Barrier Height. *Appl. Phys. Rev.* **2014**, *1*, 011304.
- (43) Acharya, J.; Wilt, J.; Liu, B.; Wu, J. Probing the Dielectric Properties of Ultrathin Al/Al<sub>2</sub>O<sub>3</sub>/Al Trilayers Fabricated Using In Situ Sputtering and Atomic Layer Deposition. *ACS Appl. Mater. Interfaces* **2018**, *10*, 3112–3120.
- (44) Wilt, J.; Gong, Y.; Gong, M.; Su, F.; Xu, H.; Sakidja, R.; Elliot, A.; Lu, R.; Zhao, S.; Han, S. Atomically Thin Al<sub>2</sub>O<sub>3</sub> Films for Tunnel Junctions. *Phys. Rev. Appl.* **2017**, *7*, 064022.
- (45) Gundlach, K.; Hölzl, J. Logarithmic Conductivity of Al–Al<sub>2</sub>O<sub>3</sub>–Al Tunneling Junctions Produced by Plasma- and by Thermal Oxidation. *Surf. Sci.* **1971**, *27*, 125–141.
- (46) Maillet, A.; Baland, B.; Peisner, J. Internal Photoemission in Ge/Sapphire/Metal Structures. *Thin Solid Films* **1983**, *109*, 225–236.
- (47) Goodman, A. M. Photoemission of Holes and Electrons from Aluminum into Aluminum Oxide. *J. Appl. Phys.* **1970**, *41*, 2176–2179.
- (48) Pollack, S.; Morris, C. Electron Tunneling through Asymmetric Films of Thermally Grown Al<sub>2</sub>O<sub>3</sub>. *J. Appl. Phys.* **1964**, *35*, 1503–1512.
- (49) DiMaria, D. Effects on Interface Barrier Energies of Metal–Aluminum Oxide-Semiconductor (Mas) Structures as a Function of Metal Electrode Material, Charge Trapping, and Annealing. *J. Appl. Phys.* **1974**, *45*, 5454–5456.
- (50) Köhler, L.; Kresse, G. Density Functional Study of Co on Rh (111). *Phys. Rev. B: Condens. Matter Mater. Phys.* **2004**, *70*, 165405.
- (51) Ma, W.; Herbert, F. W.; Senanayake, S. D.; Yildiz, B. Non-Equilibrium Oxidation States of Zirconium During Early Stages of Metal Oxidation. *Appl. Phys. Lett.* **2015**, *106*, 101603.
- (52) Puchala, B.; Van der Ven, A. Thermodynamics of the Zr–O System from First-Principles Calculations. *Phys. Rev. B: Condens. Matter Mater. Phys.* **2013**, *88*, 094108.
- (53) Pieraggi, B.; Rapp, R. A.; Hirth, J. P. Role of Interface Structure and Interfacial Defects in Oxide Scale Growth. *Oxid. Met.* **1995**, *44*, 63–79.
- (54) Jeurgens, L.; Sloof, W.; Tichelaar, F.; Mittemeijer, E. Growth Kinetics and Mechanisms of Aluminum-Oxide Films Formed by Thermal Oxidation of Aluminum. *J. Appl. Phys.* **2002**, *92*, 1649–1656.
- (55) Lambert, J.; Guthmann, C.; Ortega, C.; Saint-Jean, M. Permanent Polarization and Charge Injection in Thin Anodic Alumina Layers Studied by Electrostatic Force Microscopy. *J. Appl. Phys.* **2002**, *91*, 9161–9169.
- (56) Kornblum, L.; Meyler, B.; Cytermann, C.; Yofis, S.; Salzman, J.; Eizenberg, M. Investigation of the Band Offsets Caused by Thin Al<sub>2</sub>O<sub>3</sub> Layers in HfO<sub>2</sub> Based Si Metal Oxide Semiconductor Devices. *Appl. Phys. Lett.* **2012**, *100*, 062907.
- (57) Yeo, Y.-C.; King, T.-J.; Hu, C. Metal-Dielectric Band Alignment and Its Implications for Metal Gate Complementary Metal-Oxide-Semiconductor Technology. *J. Appl. Phys.* **2002**, *92*, 7266–7271.
- (58) Tamura, T.; Ishibashi, S.; Terakura, K.; Weng, H. First-Principles Study of the Rectifying Properties of Pt/TiO<sub>2</sub> Interface. *Phys. Rev. B: Condens. Matter Mater. Phys.* **2009**, *80*, 195302.
- (59) Zhou, Y.; Zhang, Z.; Fang, Z.; Qiu, M.; Ling, L.; Long, J.; Chen, L.; Tong, Y.; Su, W.; Zhang, Y.; Wu, J. C. S.; Basset, J.-M.; Wang, X.; Yu, G. Defect Engineering of Metal–Oxide Interface for Proximity of Photooxidation and Photoreduction. *Proc. Natl. Acad. Sci.* **2019**, *116*, 10232–10237.

- (60) Yang, Z.; Lu, Z.; Luo, G.; Hermansson, K. Oxygen Vacancy Formation Energy at the Pd/CeO<sub>2</sub> (111) Interface. *Phys. Lett. A* **2007**, *369*, 132–139.
- (61) DuBois, T. C.; Per, M. C.; Russo, S. P.; Cole, J. H. Delocalized Oxygen as the Origin of Two-Level Defects in Josephson Junctions. *Phys. Rev. Lett.* **2013**, *110*, 077002.
- (62) Kang, J.; Zhu, J.; Curtis, C.; Blake, D.; Glatzmaier, G.; Kim, Y.-H.; Wei, S.-H. Atomically Abrupt Liquid-Oxide Interface Stabilized by Self-Regulated Interfacial Defects: The Case of Al/Al<sub>2</sub>O<sub>3</sub> Interfaces. *Phys. Rev. Lett.* **2012**, *108*, 226105.
- (63) Reichel, F.; Jeurgens, L.; Richter, G.; van Aken, P.; Mittemeijer, E. The Origin of High-Mismatch Orientation Relationships for Ultra-Thin Oxide Overgrowths. *Acta Mater.* **2007**, *55*, 6027–6037.
- (64) Chase, M. W., Jr. *Nist-Janaf Thermochemical Tables*; American Chemical Society, 1998; Vol. 9.
- (65) Levin, I.; Brandon, D. Metastable Alumina Polymorphs: Crystal Structures and Transition Sequences. *J. Am. Ceram. Soc.* **1998**, *81*, 1995–2012.
- (66) Frenkel, D.; Smit, B. *Understanding Molecular Simulation: From Algorithms to Applications*; Elsevier, 2001.
- (67) Senftle, T. P.; Meyer, R. J.; Janik, M. J.; van Duin, A. C. Development of a Reaxff Potential for Pd/O and Application to Palladium Oxide Formation. *J. Chem. Phys.* **2013**, *139*, 044109.
- (68) Boutin, A.; Tavitian, B.; Fuchs, A. H. Grand Canonical Monte Carlo Simulations of Adsorption of Mixtures of Xylene Molecules in Faujasite Zeolites. *Faraday Discuss.* **1997**, *106*, 307–323.
- (69) Kresse, G.; Furthmüller, J. Efficient Iterative Schemes for Ab Initio Total-Energy Calculations Using a Plane-Wave Basis Set. *Phys. Rev. B: Condens. Matter Mater. Phys.* **1996**, *54*, 11169.
- (70) Kresse, G.; Furthmüller, J. Efficiency of Ab-Initio Total Energy Calculations for Metals and Semiconductors Using a Plane-Wave Basis Set. *Comput. Mater. Sci.* **1996**, *6*, 15–50.
- (71) Kresse, G.; Hafner, J. Ab Initio Molecular Dynamics for Liquid Metals. *Phys. Rev. B: Condens. Matter Mater. Phys.* **1993**, *47*, 558.
- (72) Medlin, D.; McCarty, K.; Hwang, R.; Guthrie, S.; Baskes, M. Orientation Relationships in Heteroepitaxial Aluminum Films on Sapphire. *Thin Solid Films* **1997**, *299*, 110–114.
- (73) Cheng, Z.; Koh, Y. R.; Ahmad, H.; Hu, R.; Shi, J.; Liao, M. E.; Wang, Y.; Bai, T.; Li, R.; Lee, E. Thermal Conductance across Harmonic-Matched Epitaxial Al-Sapphire Heterointerfaces. *Commun. Phys.* **2020**, *3*, 115.
- (74) Thompson, A. P.; Aktulga, H. M.; Berger, R.; Bolintineanu, D. S.; Brown, W. M.; Crozier, P. S.; in't Veld, P. J.; Kohlmeyer, A.; Moore, S. G.; Nguyen, T. D. Lammmps-a Flexible Simulation Tool for Particle-Based Materials Modeling at the Atomic, Meso, and Continuum Scales. *Comput. Phys. Commun.* **2021**, *271*, 108171.
- (75) Shan, B.; Cho, K. Ab Initio Study of Schottky Barriers at Metal-Nanotube Contacts. *Phys. Rev. B: Condens. Matter Mater. Phys.* **2004**, *70*, 233405.
- (76) Zhu, W.; Kaxiras, E. Schottky Barrier Formation at a Carbon Nanotube-Metal Junction. *Appl. Phys. Lett.* **2006**, *89*, 243107.